

# **Understanding the nanoscale structure of hexagonal phase lyotropic liquid crystal membranes**

Benjamin J. Coscia,<sup>†</sup> Richard D. Noble,<sup>†</sup> Douglas L. Gin,<sup>†,‡</sup> Joe Yelk,<sup>¶</sup> Matthew A. Glaser,<sup>¶</sup> Xunda Feng,<sup>§</sup> and Michael R. Shirts<sup>\*,†</sup>

<sup>†</sup>*Department of Chemical and Biological Engineering, University of Colorado Boulder,  
Boulder, CO 80309, USA*

<sup>‡</sup>*Department of Chemistry and Biochemistry, University of Colorado Boulder, Boulder CO  
80309, USA*

<sup>¶</sup>*Department of Physics, University of Colorado Boulder, Boulder CO, 80309, USA*

<sup>§</sup>*Department of Chemical and Environmental Engineering, Yale University, New Haven,  
Connecticut 06511, USA*

E-mail: michael.shirts@colorado.edu

## Abstract

Nanostructured porous membranes made from the cross-linked hexagonal phase of self-assembled lyotropic liquid crystals (LLCs) are a promising material for selective separations. In this work, we develop an atomistic molecular model of an LLC membrane. We show that our model is maximally consistent with experimental observations by comparing simulated X-ray Diffraction (XRD) patterns and calculated ionic conductivity to their experimental counterparts. We explore, in depth, the composition and structure of the nanopores in order to give insights that are not easily accessible to experimentalists. The clearer picture of the nanoscopic structure of these membranes provided in this study will enable a better understanding of the mechanisms of small molecule transport within these nanopores.

## 1 Introduction

A highly selective membrane would be useful for the recovery of valuable products from complex aqueous and organic solutions. For example, flowback water (FW) produced during hydraulic fracturing is a complex wastewater full of potentially valuable dissolved organic compounds such as acetate.<sup>1</sup> There is increasing pressure to reuse hydraulic fracturing water rather than dispose of it in order to reduce social and environmental impacts as well as cost.<sup>2</sup> Rather fully than dispose of the wastestream generated in the recycling process, we can instead use highly selective membranes in order to successfully recover useful compounds.

Current commercial RO and NF membranes suffer limitations to there selectivity which is inherent to their fabrication. Although scalable, each of these two types of membranes has a degree of stochasticity that makes overcoming well-known the permeability-selectivity tradeoff a challenge. Namely, it is difficult to increase the permeability of a desired molecular or atomic species, while maintaining the same retention of an undesired species.<sup>3</sup>

Selective separation by a semipermeable membrane barrier is a function of the geometric and chemical interactions of solutes with the membrane material. A molecule's size, shape,

charge and polarity combine to determine the degree to which a solute partitions into a membrane and how fast it travels through the membrane. To separate a component from a mixture, one must understand how to design membranes in order to tune the relative transport rates of desired and undesired solutes.<sup>4,5</sup>

Crosslinked lyotropic liquid crystal (LLC) membranes may be capable of performing highly selective separations. LLCs are amphiphilic molecules that have the ability to self-assemble into porous nanostructures<sup>6</sup> which can be crosslinked to create mechanically strong membrane films with pores on the order of 1 nm in diameter.<sup>7</sup> Unlike most commercial NF membranes, LLC membrane pores are uniform in size. Since LLC membranes lack a pore size distribution, they inherently exhibit high selectivity due to their strict molecular weight cut-off (MWCO).<sup>7</sup> Additionally, the LLC monomers described in this paper are salts, and therefore lead to Donnan exclusion of ions in solution. The membrane gains a net surface charge when counterions from the head groups that line the pore walls escape into the feed solution in order to balance the gradients of concentration and electric potential.<sup>8</sup>

The feasibility of LLC membranes has been demonstrated using LLCs that form the type I bicontinuous cubic ( $Q_I$ ),<sup>9–11</sup> and the inverted hexagonal ( $H_{II}$ )<sup>7</sup> phases (See Figure 1). When separating organic solutes from NaCl,  $Q_I$  phase membrane filtration experiments have shown selectivity 2–3 times higher than commercial RO and 6–12 times higher than commercial NF membranes.<sup>1</sup> When separating a series of various sized dyes, the  $H_{II}$  phase membrane showed complete rejection of dyes bigger than 1.2 nm in size.<sup>7</sup>

The  $H_{II}$  phase pore geometry is has a higher theoretical capacity for transport than the  $Q_I$  phase. The  $H_{II}$  phase forms at room temperature in the presence of c.a. 10 wt% water and consists of hexagonally packed, hydrophilic pore columns.<sup>6</sup> In the absence of water, neat monomer will form the same hexagonal columnar structure which, in literature, has been referred to as the  $Col_h$  thermotropic phase<sup>12</sup> (See Figure 1b). The most promising  $Q_I$  phase for membrane applications forms at 70°C when monomer is mixed with c.a. 20 wt% glycerol.<sup>11</sup>  $Q_I$  phase membranes consist of a tortuous network of three dimensionally interconnected

pores that prevent optimal through-plane transport. The densely packed, non-tortuous and uniform sized pores of  $H_{II}$  phase membranes represent the ideal geometry for achieving high solute flux.<sup>13</sup> Despite the promise of the  $H_{II}$  phase, the hexagonally packed liquid crystalline domains, formed when Na-GA3C11 monomers self-assemble, are isotropically aligned which is detrimental to membrane permeability.

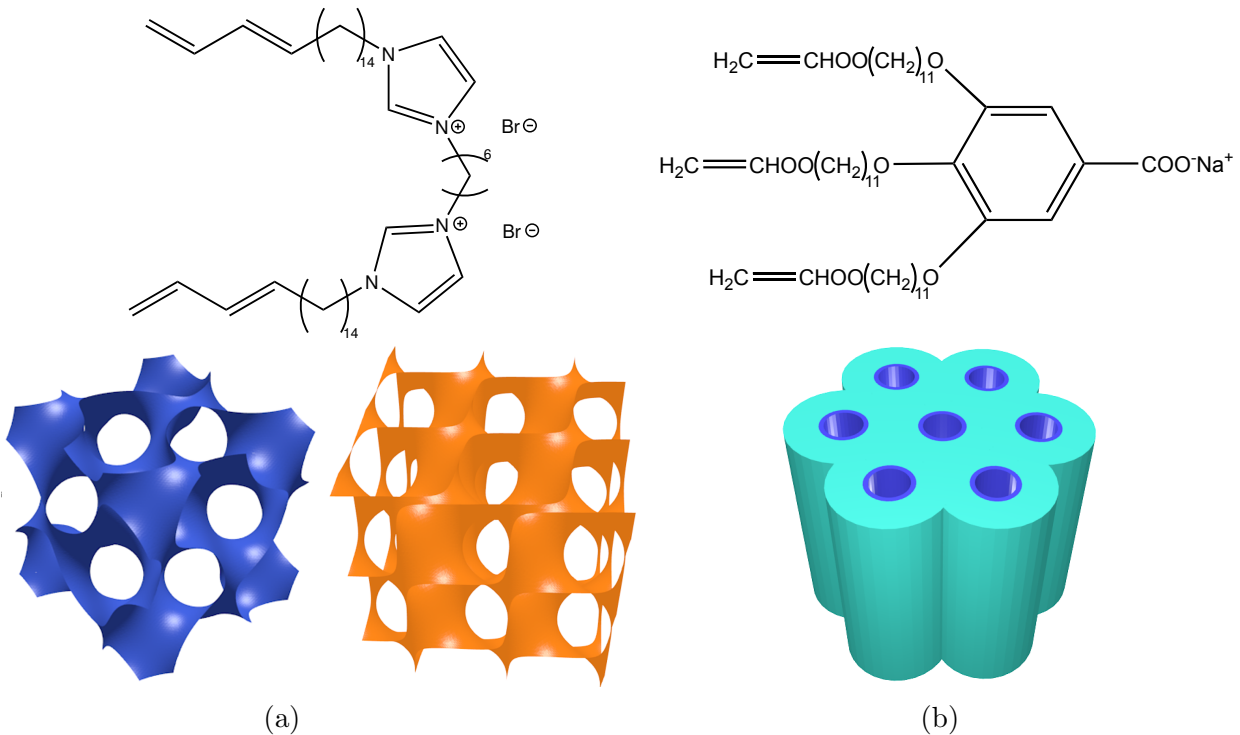


Figure 1: The choice of LLC monomer and solvent leads to different accessible liquid crystalline phases. The monomer shown in (a) forms the  $Q_I$  phase in either the  $Ia3d$  (left) or  $Pn3m$  (right) space group. The surfaces shown represent the interface between the hydrophilic and hydrophobic regions of the unit cell. As pictured, we assume that each region occupies an equal volume. The monomer shown in (b) will form the hexagonal columnar phase ( $H_{II}$  in the presence of water or  $Col_h$  when no water is present). The blue region represents the hydrophilic pores while the cyan region represents the surrounding hydrophobic monomer tails.

Recently, researchers have learned how to macroscopically align the hexagonal domains which has revived research into  $H_{II}$  phase LLC membranes. Previously, research efforts were focused on the  $Q_I$  phase, whose geometry does not require alignment. In 2014, Feng et al. showed that one can align  $Col_h$  hexagonal domains using a magnetic field with subsequent

cross-linking to lock the structure in place.<sup>12</sup> In 2016, Feng et al. showed that one could obtain the same result using a second technique termed soft confinement.<sup>14</sup> Current efforts are focused on extending the method to the H<sub>II</sub> phase and characterizing the performance of these newly aligned systems.

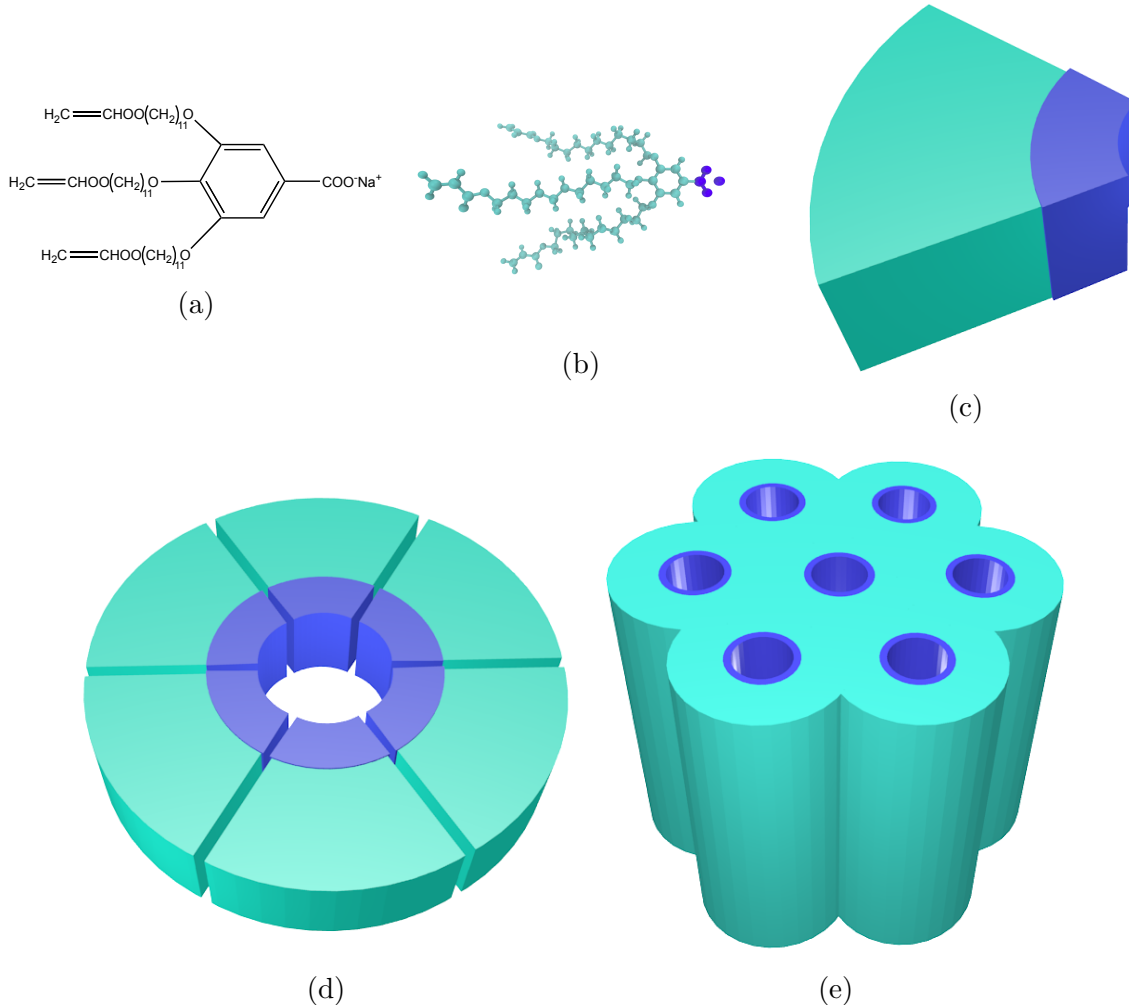


Figure 2: The LLC monomer Na-GA3C11 (a) rendered atomistically (b) exhibits wedge-like character (c). Monomer wedges assemble into disks (d) with hydrophilic head groups (blue) facing towards the disk center. The disks assemble into hexagonally packed columnar mesophases (e).

Our current understanding of the molecular details of LLC membrane nanostructure is not sufficient to be able to precisely design them for specific separations. Over the past 20 years, H<sub>II</sub>-phase LLC polymer membrane studies have been limited primarily to Na-GA3C11

with some characterization done after minor structural modifications. Resel et al. varied the length of the monomer tails and the counterion used and observed its affect on pore spacing.<sup>15</sup> In a later study of rejection performance, it was shown that membranes formed by cross-linked Na-GA3C11 in the H<sub>II</sub> phase cannot separate solutes less than 1.2 nm in diameter because the pores are too large.<sup>7</sup> We do not yet understand how to controllably reduce the effective pore size or how to tune the chemical environment in the nanopores of this or related materials for small molecule separations. The only source of predictive modeling for LLC systems have been macroscopic models that likely do not adequately describe transport at these length scales.<sup>9</sup> It will be challenging to efficiently narrow down the large design space in a laboratory setting without a robust model.

A molecular-level understanding of LLC polymer membrane structure, enabled by molecular dynamics (MD) simulations, can provide guidelines to reduce the large chemical space available to design monomers for creation of separation-specific membranes. A good molecular model should incorporate a detailed picture of the nanoscopic pore structure which will be crucial to understanding the role of monomer structure in solute transport and membrane design. Models resulting from molecular dynamics simulations will provide the required level of detail (Fig. 3), assuming the force fields are sufficiently accurate. With such an atomistic model, we can directly observe molecular-level solute transport and suggest governing mechanisms. We can observe how the choice of head group interacts with solutes of interest. We can interchange counterions which may influence both the pore size and the strength of the Donnan potential.

In this study, we build a significantly more realistic atomistic model of LLC membranes than, to our knowledge, has ever previously been created, and explore what new structural information can be gained and what structure hypotheses are supported by this model. We validate the model using as much experimental information as possible. We are most interested in reproducing the conclusions about structure drawn from small angle X-ray scattering (SAXS) and wide angle X-ray scattering (WAXS) experiments as well as in matching ionic

conductivity measurements.<sup>14</sup>

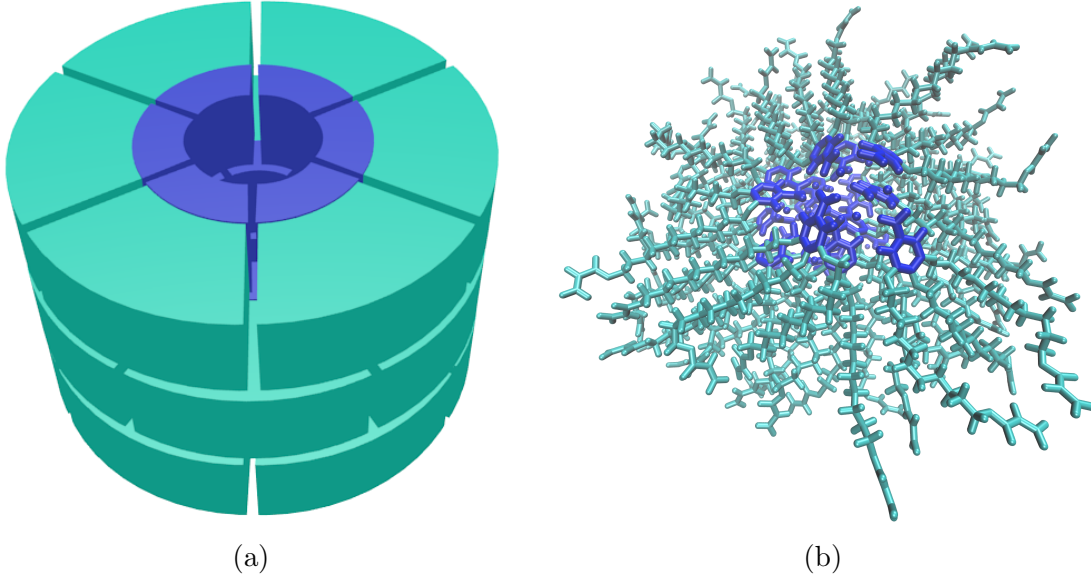


Figure 3: One can only speculate about solute behavior inside the membrane pores based on the previously established picture of the pore structure (a). We use a detailed molecular model in order to appropriately model the pore’s complex architecture which is crucial to understanding the mechanism of solute transport (b). The head group region is colored blue and the tail region is colored cyan in both representations. This image was generated from the molecular simulations run for this paper.

Here we develop a molecular model of the Col<sub>h</sub> assembly formed by Na-GA3C11. Compared to the H<sub>II</sub> phase, the Col<sub>h</sub> phase is a simpler starting point. The system has no water which will allow us to simulate longer timescales, and there exists detailed experimental characterization of the fully aligned state, including 2D wide-angle X-ray scattering (WAXS) patterns (Figure 4b) which are useful for reconstructing structural data. We will use this Col<sub>h</sub> model in order to build an H<sub>II</sub> model in the future.

There are five major features of interest present in the 2D experimental pattern shown in Figure 4b.

1. *R*- $\pi$ : The location of the first is at  $q_z = 1.7 \text{ \AA}^{-1}$ , corresponding to a real space separation of 3.7 Å. Previous work<sup>12</sup> attributes this reflection to  $\pi$ - $\pi$  stacking between aromatic

rings in the direction perpendicular to the membrane plane, or z-axis.<sup>12</sup> For simplicity, we will refer to this reflection as R- $\pi$ .

2. *R-double*: A weak intensity line, located at exactly half the  $q_z$  value of R- $\pi$  ( $q_z = 0.85 \text{ \AA}^{-1}$ ), corresponds to a real space periodic spacing of  $7.4 \text{ \AA}$ . Since this reflection corresponds to double the spacing of R- $\pi$  in real space, will refer to this reflection as R-double. R-double has been interpreted as  $2_1$  helical ordering of aromatic rings along the z axis,<sup>12</sup> meaning that if one traces the positions of the aromatic rings with a helical curve, then for each full turn in the helix, one will encounter two aromatic rings.
3. *R-alkanes*: A low intensity ring located at  $r = 1.4 \text{ \AA}^{-1}$  marks the third major reflection of interest. The real space separation corresponds to  $4.5 \text{ \AA}$  which is characteristic of the average spacing between packed alkane chains.<sup>16</sup> We will call this reflection R-alkanes.
4. *R-spots*: Within R-alkanes, are four spots of higher relative intensity. Accordingly, we name these reflection R-spots. The location of all spots is  $\sim 37^\circ$  from the  $q_z$  axis in their respective quadrants. In many liquid crystal systems one can explain the spots as the tilt angle of the alkane chains with respect to the membrane plane.<sup>17</sup>
5. *R-pores*: The final feature corresponds to the spacing and symmetry of the  $d_{100}$  plane. This plane is geometrically related the distance between pores. The feature, which we named R-pores, is characterized by dots along the equatorial axis defined when  $q_z = 0$ . The spacing between dots is indicative of the hexagonal symmetry of the packed pores. We observe the same information with higher resolution using SAXS (Fig. 4a).

Despite having structural data, there is still information which experiment cannot definitively answer. There are a number of structural questions we wish to answer in this article. We want to know:

1. What is the density of monomers that pack around each hydrophilic core?

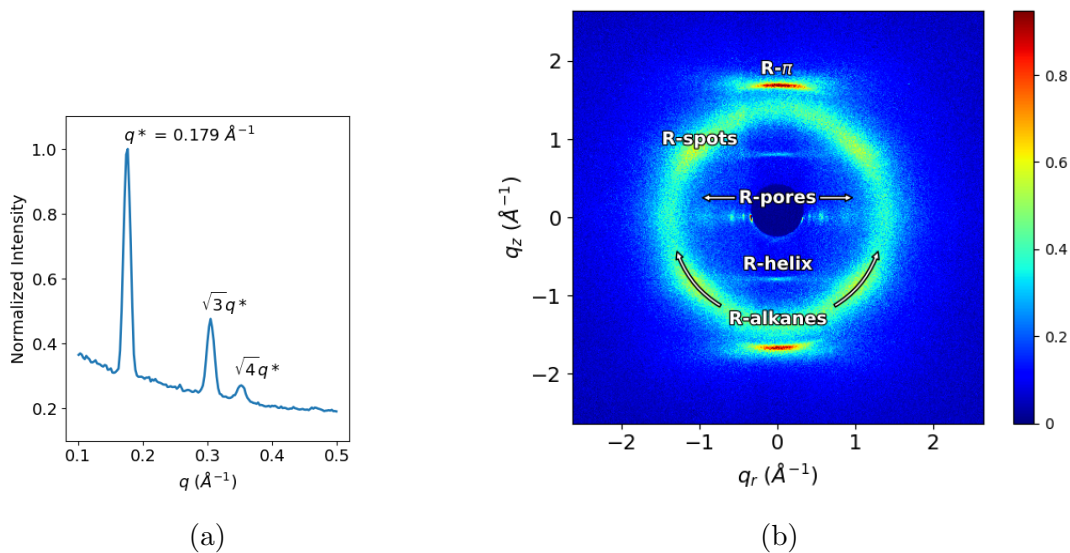


Figure 4: (a) (Reproduced from<sup>14</sup>) The repeat spacing in the 1D small angle X-ray scattering pattern is characteristic of hexagonal packing. The leading peak,  $q^*$ , represents the distance between the  $d_{100}$  planes. Using this distance, we know that the distance between pore centers is 4.12 nm. (b) 2D WAXS gives details about repeating features on the order of angstroms. Experimentalists have explained each of the 5 major reflections present as follows: (R- $\pi$ ) Aromatic head groups  $\pi - \pi$  stack 3.7  $\text{\AA}$  apart. (R-double) Monomers arrange vertically in a  $2_1$  helix. (R-alkanes) Alkane chain tails pack 4.5  $\text{\AA}$  apart. (R-spots) Monomer tails are tilted with respect to the membrane plane. (V) As derived from SAXS, the pores are spaced 4.12 nm apart and pack hexagonally

Authors often describe this and similar systems as being made up of layers. A simple molecular simulation study of a similar molecule suggested that there are 4 monomers in each layer. Their estimation is based on a simulated system containing only 16 total monomers which likely does not sufficiently model the chemical environment present in the real system.<sup>18</sup> A separate calculation based on the volume of the liquid crystal monomers proposes that there are seven monomers in each layer.<sup>15</sup>

We are careful to avoid the term 'layers' since a liquid crystalline system has, by definition, long range order in 1 or 2 spatial dimensions and short range order in the other dimensions.<sup>19</sup> In the system we are studying, there are long-range 2D correlations in the hexagonal array of pores (xy plane) and short range correlations in the z-direction. We will use our atomistic molecular model to study how the system's structure is effected by the density of monomers surrounding each pore's hydrophilic core.

## 2. What structural motif best matches experimental 2D WAXS patterns?

On the short timescales accessible to MD, we observe distinct metastable configurations which depend on starting configuration. We simulated XRD patterns of our system and compared them to experimental 2D WAXS patterns (Figure 4b so that we ensure our model creates a nanoscopic chemical environment maximally consistent with experiment within the constraints of our forcefield. Using this approach, we are able to confirm some previous interpretations of the WAXS pattern and refute others.

## 3. What is the chemical composition of the pores?

The limited picture that experiment provides tells us that there are hexagonally packed, hydrophilic regions where transport is likely to occur. One may instinctively imagine these regions as tube-like pathways with well-defined boundaries. We will explore the composition of the pores, the partition between the hydrophilic and hydrophobic regions, and its sensitivity to initial configuration.

## 4. Is it necessary to include any water in order to appropriately model the Col<sub>h</sub> phase?

While the Col<sub>h</sub> phase is described as dry, it is likely that small amounts of ambient water may be leached into the system. The hydrogen bonding network formed by the water may play a role in structuring the pore. We used simulated X-ray diffraction patterns to see if there is any meaningful structural difference between a "dry" and "wet" system.

## 2 Methods

### 2.1 Monomer Parameterization

We parameterized the liquid crystal monomer Na-GA3C11 using the Generalized AMBER Force Field (GAFF)<sup>20</sup> with the Antechamber package<sup>21</sup> provided with AmberTools16.<sup>22</sup> We assigned atomic charges using the am1bccsym method of `molcharge` shipped with QUACPAC from Openeye Scientific Software. We ran all molecular dynamics simulations using Gromacs 2016.<sup>23-26</sup>

We generated an ensemble of characteristic, low-energy vacuum monomer configurations by applying a simulated annealing process to a parameterized monomer. We cooled monomers from 1000K to 50K over 10 nanoseconds. We randomly pulled a low energy configuration from the trajectory then reassigned charges using `molcharge`. Using the new charges, we annealed the monomer system again and pulled a random monomer configuration from the trajectory which we used for full system construction (Figure 5a). See section S-2 for further detail.

### 2.2 Unit Cell Preparation

The timescale for self-assembly of monomers into the hexagonal phase is unknown and likely outside of a reasonable length for an atomistic simulation, calling for a more efficient way to build the system. Previous work has shown a coarse-grained model self assemble into the H<sub>II</sub> phase configuration in  $\sim$ 1000 ns.<sup>27</sup> We attempted atomistic self-assembly by packing

monomers into a box using Packmol.<sup>28</sup> Simulations of greater than 100 ns show no indicators of progress towards an ordered system (See section S 1). To bypass the slow self-assembly process, we use Python scripts to assemble monomers into a structure close to one of a number of hypothesized equilibrium configurations (Figure 5).

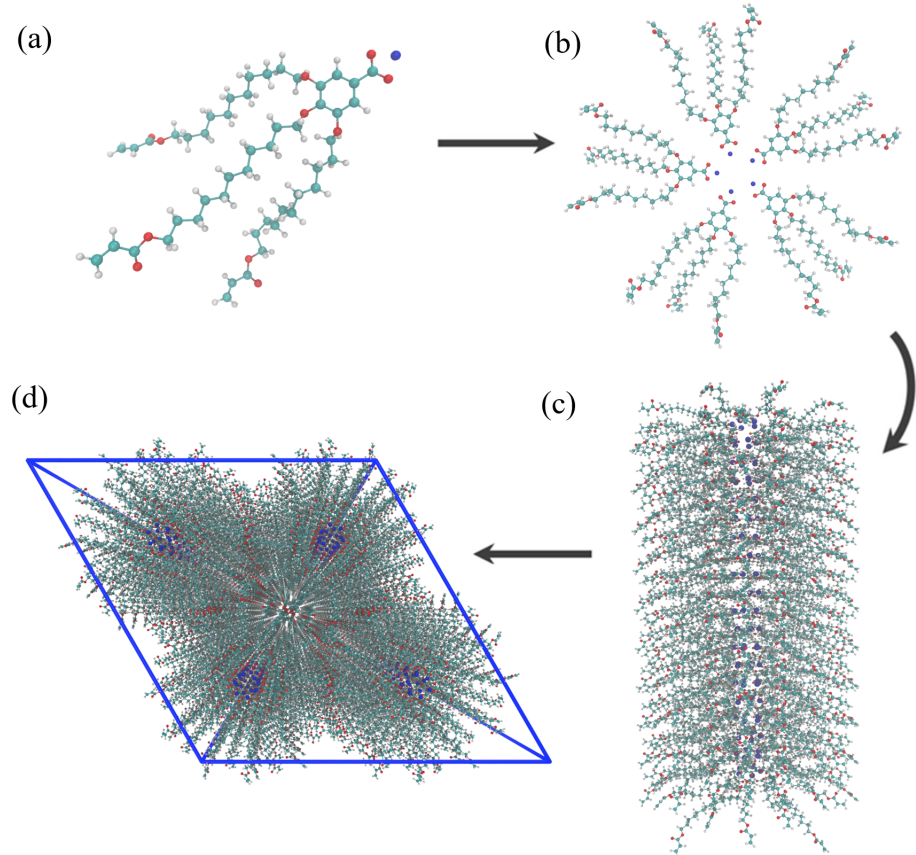


Figure 5: (a) We parameterized a single monomer and annealed it to produce a low energy configuration. (b) A Python script assembles monomers into columns which are duplicated and rotated to surround hydrophilic pore centers. (c) We chose to stack twenty monomers into each column. (d) The pores are duplicated and placed into a monoclinic unit cell.

A typical simulation volume contains four pores in a monoclinic unit cell, the smallest unit cell that maintains hexagonal symmetry when extended periodically. Each pore is made of columns of stacked monomers with periodic continuity along the pore axis, avoiding any edge effects and creating an infinite length pore ideal for studying transport. We prefer a small number stacked monomers in order to reduce computational cost and to allow us to look at longer timescales. Ultimately, we chose to build a system with 20 monomers per

column in order to obtain sufficient resolution when simulating X-ray diffraction patterns.

## 2.3 Monomer Placement

When constructing an initial configuration, there are a number of variables which require careful consideration while placing monomers. The equilibrium configuration is sensitive to some while insensitive to others. The starting pore radius, defined as the distance of a chosen head group carbon from the pore's central axis, does not influence the equilibrium structure if one chooses a reasonable value. The pore radius is chosen to be 0.5 nm in our initial configurations. The initial distance between pores, within a wide range, also has little effect on the equilibrated structure. However, one should not start them too close or there will be high energy repulsions during early equilibration. We chose an initial pore spacing of 4.5 nm,  $\sim 10\%$  larger than the experimental value of 4.12 nm. A sensitivity analysis of both parameters is presented in the Supporting information, section S-4. The distance between vertically stacked monomers, the position of monomers with respect to vertically adjacent monomers, and the number of columns per pore do influence the equilibrated structure and require further justification for their choices. We rely on experimental data to inform them.

We chose the vertical spacing between monomers for the initial configuration based on  $R-\pi$  and then allowed the system to readjust during equilibration. Each monomer was rotated so the plane of its aromatic head groups would be coplanar with the xy plane. We explored three different initial monomer spacings. The first is exactly equal to  $R-\pi$  with layers placed so aromatic rings stack 3.7 Å apart in the z-direction. We explore a second system with an initial spacing of 5 Å. We briefly explored a third system with an initial spacing of 10 Å, however it shows non-physical behavior which is detailed in the Supporting Information, section S-4.3.

We chose the relative orientation between vertically adjacent monomers in each column based on clues from diffraction data as well as the various known stacking modes of benzene and substituted benzene rings: sandwiched, parallel-displaced and T-shaped.<sup>29</sup> We ruled out

the T-shaped configuration because its  $\sim 5$  Å equilibrium stacking distance<sup>29</sup> is inconsistent with  $R\text{-}\pi$ . It is also infeasible for the monomers to orient in the T-shaped conformation because of the bulky tail groups. We will explore the system’s preference towards the sandwiched vs. parallel displaced stacking modes in some detail. Both have reported stacking distances near the  $R\text{-}\pi$  value of 3.7 Å. Head groups in our sandwiched initial configuration stack directly on top of each other while head groups in the parallel displaced initial configuration stack with an offset of  $180^\circ/ncol$  where  $ncol$  is the number of columns per pore. See the Supporting Information, Figure 4 for a detailed illustration of the initial configurations in each mode.

The number of columns per pore is unknown, as stated in question (1). We tested configurations constructed with a varied number of columns per pore. We built systems in the offset and parallel displaced configurations with 4, 5, 6, 7 and 8 monomers per layer.

## 2.4 Equilibration

We developed equilibration schemes to create dry and wet configurations. Both schemes start with an initial configuration generated according to the previous guidelines. To create a dry configuration, we fix monomer head groups in the sandwiched or parallel-displaced configuration using position restraints with a force constant of  $10^6$  kJ mol $^{-1}$  nm $^{-2}$ . We run a 50 ps simulation in the NVT ensemble which allows the monomer tails to settle without disrupting the ordering of the head groups. Doing so also mitigates system dependence on initial monomer configuration. Every 50 ps, we reduce the force constants by the square root of its previous value. Once the force constant is below 10 KJ mol $^{-1}$  nm $^{-2}$ , we reduce the restraints in a sequence with values of 8, 3, 2, 1, and 0 KJ mol $^{-1}$  nm $^{-2}$  respectively. We allow the resulting unrestrained structure to equilibrate for 5 ns in the NPT ensemble with pressure controlled by the berendsen barostat. Next, we run long NPT equilibration simulations for at least 400 ns using the Parrinello-Rahman barostat with a time constant of 10 ps.

In order to create a “wet” system, we solvated an initial configuration with water using `gmx solvate`. We remove all water molecules placed outside the pore region. Then we randomly remove water molecules inside the pore region until the pores reach the desired concentration of water. The remainder of the equilibration follows the same procedure as the dry system.

## 2.5 Equilibrium Calculations

### 2.5.1 *Determining equilibration time*

Using equilibrated structures, we carry out various calculations to characterize the system. We define the point at which a system is equilibrated based on when the distance between pores stops changing. We determined when the distances stopped changing by applying the statistical test, `pymbar.timeseries.detectEquilibration`, to the time series.<sup>30,31</sup> Simulations of 400 ns give at least 50 ns of equilibrated simulation trajectory.

### 2.5.2 *Calculation of pore spacing*

To calculate the equilibrated pore spacing, we measured the distance between pore centers. We located the pore centers by averaging the coordinates of sodium ions in their respective pores. We generated pore spacing statistics using the bootstrapping technique (See section S-3 of the Supporting Information).

### 2.5.3 *Pair distribution functions and correlation length*

The normalized pair distribution function,  $g(\mathbf{r})$ , describes the probability of finding a pair of particles separated by  $\mathbf{r}$ ,

$$g(\mathbf{r}) = \frac{1}{\rho N} \left\langle \sum_{i=1}^N \sum_{j \neq i}^N \delta(\mathbf{r} + \mathbf{r}_j - \mathbf{r}_i) \right\rangle \quad (1)$$

where  $\rho$  is the average number density of particles and  $\delta(\mathbf{r})$  is the Dirac delta function.<sup>32</sup> We applied equation 1 in three dimensions and then extracted one dimensional distribution functions using slices of the grid along the appropriate axis.

We measured the one dimensional pair distribution function,  $g(z)$ , between centers of masses of aromatic head group rings along the z-axis (perpendicular to the membrane plane). We averaged all 1D slices in the z-direction of the full 3D correlation function within 2.1 Å of  $(x, y) = (0, 0)$ . We chose 2.1 Å as a crude approximation of the radius of the phenyl ring plane. We calculated the radius as the sum of the longest C-C distance within a phenyl ring (2.8 Å) and two times the carbon atom radius (0.7 Å).

Here,  $g(z)$  is characterized by an oscillatory function with a period equal to the average distance between stacked monomers, and an amplitude that decays exponentially (See Figure 13). The rate of decay is related to the correlation length, L, between monomer head groups. We estimated L by fitting the peaks of  $g(z)$  to a decaying exponential function of the form:

$$Ae^{-z/L} \quad (2)$$

where A is a fitting parameter for amplitude, z is the independent variable of  $g(z)$  and L is the fit correlation length. The error in the estimated value of L is calculated as the square root of the diagonal entry of the covariance matrix of optimized fit parameters.

We also used  $g(z)$  to calculate the equilibrated vertical stacking distance between monomers,  $d_{equil}$ . We fit a decaying sinusoidal function to  $g(z)$  of the form:

$$1 - A\cos\left(\frac{2\pi}{d_{equil}}z + B\right)e^{-z/L} \quad (3)$$

where A and B are fit parameters for the function's amplitude and phase shift respectively. This function could be used in place of Equation 2, however it does not fit the peaks of  $g(z)$  from parallel displaced configurations well enough to extract a reliable value of L.

#### **2.5.4 Radial distribution functions**

We explored the pores' compositions by measuring the average number densities of various monomer components as a function of distance from the pore centers. We looked at the average number density of sodium ions, aromatic rings and carbon atoms making up the monomer tails. We binned the radial distance of all atoms in each group from the pore centers, then normalized by the volume of the annulus defined by the bin edges and the z box vector (See Figure 18 in the Supporting Information).

#### **2.5.5 Simulated structure factor calculations**

Simulated X-ray diffraction patterns were generated based on atomic coordinates in order to make a direct experimental comparison. All atomic coordinates were simulated as Gaussian spheres of electron density corresponding to each atom's electronic radius. A three dimensional Fourier transform (FT) of the array of electron density results in a three dimensional structure factor which represents the unit cell in reciprocal space. The experimental WAXS measurement was made using a vertically aligned film whose pores were oriented perpendicular to the direction of the incident X-ray beam. Although the pores were vertically aligned, the crystalline domains were still misaligned with respect to the xy plane. To account for this, we averaged 2D slices of the structure factor at all angles about  $|\mathbf{q}| = (0, 0, z)$ .

We normalized all diffraction patterns relative to R-alkanes. We believe that the alkane-alkane density, averaged over all angles, is the feature most likely to be replicated between experiment and simulation. Other features are dependent on system ordering which is likely to have some dependence on initial configuration. We calculated the average intensity within R-alkanes of the experimental pattern,  $I_{avg}$  and divide all intensities by this values. In this way, the average intensity of the alkanes is equal to 1. When calculating  $I_{avg}$ , we excluded intensities within  $\pm 30^\circ$  of the meridional axis defined by  $q_r = 0$ , since the simulated patterns differ from experiment in those regions in all cases. Specifically, in contrast to the experimental WAXS pattern, R- $\pi$  appearing in simulated diffraction patterns intersects with

R-alkanes (See Fig. 8). We set an upper bound on the colorbar by multiplying  $I_{avg}$  by a scaling factor,  $f$ . Intensities that appear in the patterns  $\geq f \times I_{avg}$  are colored uniformly. We apply the same scaling method to the simulated patterns. We carefully chose a scaling factor of  $f = 3.1$  in order to visibly display all features in the all patterns.

### 2.5.6 *Ionic conductivity calculations*

We calculated ionic conductivity using two different methods for robustness. The Nernst-Einstein relation, relates the DC ionic conductivity,  $\sigma$ , to ion diffusivity,  $D$ , concentration,  $C$ , ion charge,  $q$ , the Boltzmann constant,  $k_b$ , and temperature,  $T$ :

$$\sigma = \frac{q^2 C D}{k_b T} \quad (4)$$

We measured sodium ion diffusion coefficients by calculating the slope of the linear region of the z-direction mean square displacement curve as indicated by the Einstein relation.<sup>33</sup> We visualized the MSD plot to determine where to begin and end a linear fit. We measured ion concentration with respect to the volume of the entire unit cell. The second method, termed the Collective Diffusion model, measures the movement of the collective variable,  $Q$ , which is defined as the amount of charge transfer through the system and can be thought to represent the center of charge of the system. The conductance,  $\gamma$ , of the system can be calculated as:

$$\gamma = \frac{D_Q}{k_b T} \quad (5)$$

We convert the resulting value to ionic conductivity by multiplying by channel length and dividing by the membrane cross sectional area.  $D_Q$  is the diffusion coefficient of the collective variable  $Q$ . It is calculated using the Einstein relation. One can access a detailed derivation of the model elsewhere.<sup>34</sup>

## 2.6 Cross-linking

In order to fully match synthetic procedures, we created a cross-linking algorithm that one can apply to equilibrated structures. The purpose of cross-linking is to maintain macroscopic alignment of the crystalline domains, ensuring aligned, hexagonally packed pores. For that reason, we are not concerned with replicating the kinetics of the reaction, but instead emphasize the consistency of the final structure with experimental structural data.

We developed the algorithm based on the known reaction mechanism. Cross-linking of this system is a free radical polymerization (FRP) taking place between terminal vinyl groups present on each of the three monomer tails. The reaction mechanism is drawn out in Figure S-22. FRPs require an initiator which bonds to the system, meaning new atoms are introduced into the system. For simplicity, we simulated the initiator as hydrogen and made it present in the simulation by including them as dummy atoms in all possible locations where an addition could occur. We carry out the cross-linking procedure iteratively. During each iteration, the algorithm selects eligible bonding carbon atoms based on a distance cut-off. The topology is updated with new bonds and dummy hydrogen atoms are changed to appropriate hydrogen types. Head-to-tail addition was the only propagation mode considered due to its dominance in the real system.<sup>35</sup> We did not consider direction of attack because the resultant mixture is racemic.

Our implementation requires long simulation times to achieve high cross-link densities. A typical cross-linking procedure can take up to 24 hours. In order to collect equilibrated data, further NPT simulation is necessary. We typically run a cross-linked system for an additional 100 ns to allow the system to readjust. For those reasons we did not cross-link all systems tested, but only the most promising structures. We show that cross-linking does not significantly change any of our drawn conclusions in Section 3.6.

## 3 Results and Discussion

### 3.1 Density of monomers around pores

Our simulations best support a model built with 5 monomer columns per pore based on the measured equilibrated pore-to-pore distances. To discern the composition of the monomer layers, addressing question (1), we ran simulations of systems created with 4–8 columns per pore. We built systems in both the parallel displaced and sandwiched configurations and equilibrated them according to the dry equilibration procedure. We tested all systems with an initial vertical monomer spacing,  $d$ , of 3.7 Å in accordance with R- $\pi$ . We tested 4 additional systems with monomers initially spaced 5 Å apart vertically (See section 4.1 of the supporting info for more details on sensitivity to initial layer spacing). The pore-to-pore spacing was considered equilibrated, as defined in section 2.5.1, in all systems after 400 ns of simulation. Figure 7 shows the equilibrated pore-to-pore distances for all systems tested.

All systems tested, although equilibrated from the perspective of the metrics used here, are frozen in metastable basins. Not all make physical sense or fit the experimental profile that we are trying to match. In the limit of infinite simulation time, all systems will converge to a single equilibrium configuration. For simplicity, we will group the systems studied here into the ordered and disordered basins. Any system where  $d = 3.7$  Å will be included in the ordered basin and any system where  $d = 5.0$  Å will be included in the disordered basin. The reason for these names will become clearer as we progress through our analysis.

Systems built with 5 columns in each pore equilibrate to a pore spacing that is most consistent with the experimental value of 4.12 nm derived from SAXS measurements (Figure 4a). The remainder of this discussion will focus on the analysis of systems built with 5 columns per pore. Ordered basin systems built with 6 columns per pore, have an equilibrated pore spacing c.a. 0.50 nm higher than experiment. Ordered basin systems built with 4 columns per pore equilibrate to an average pore spacing 0.25 nm lower than experiment.

Disordered basin systems built with 6 columns-per-pore are not compact in the z-direction.

The final pore spacing is close to experiment within its uncertainty. Relative to ordered basin 6 column-per-pore systems, the unit cell is elongated in its z dimension and contracted in its x and y dimensions, however the box volume stays nearly constant in all cases (Figure 6). The system is likely not fully equilibrated and may eventually rearrange into something that resembles a 5 column-per-pore system. Further investigations into this are beyond the scope of this paper.

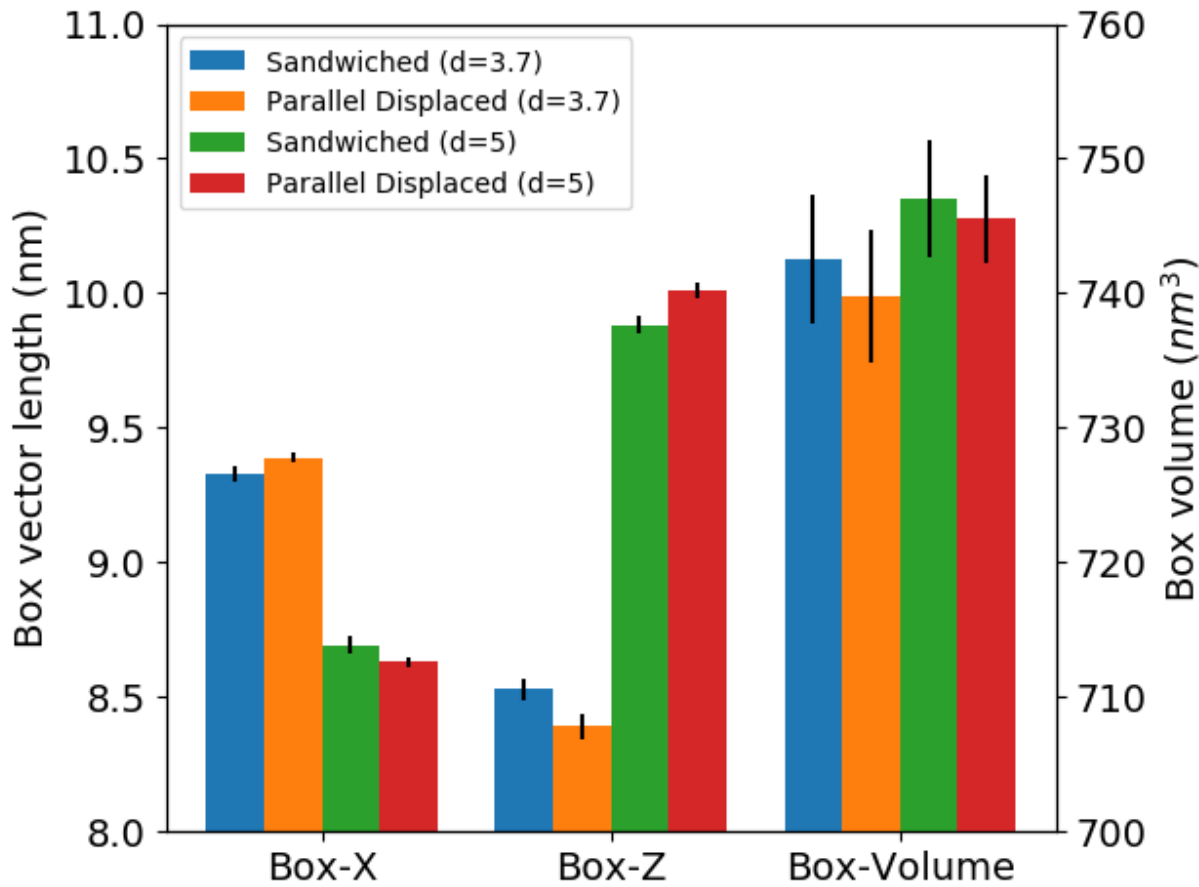


Figure 6: When monomers are initially stacked 5 Å apart ( $d = 5\text{\AA}$ ), the unit cell expands in the z direction and contracts in its x and y dimensions. The volume remain nearly constant across all cases. The y dimension box vectors are not included since we use semiisotropic pressure coupling which requires that the x and y box vectors change uniformly.

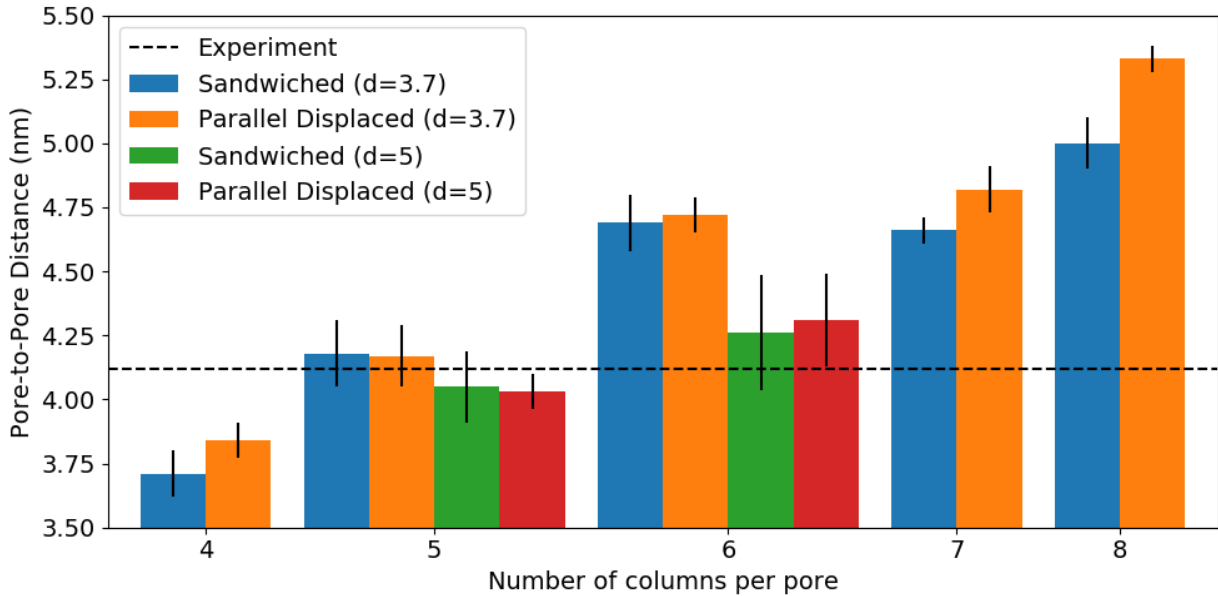


Figure 7: Systems with 5 columns per pore have equilibrated pore spacings closest to the experimental value of 4.12 nm. The equilibrated pore spacing of the model increases as the number of columns in each pore increases.

### 3.2 Structural refinement with 2D WAXS data

We further refined our structural understanding of the system by simulating X-ray diffraction patterns produced from equilibrated MD trajectories and comparing them to experiment. We tested systems built with 5 columns per pore in the parallel displaced and sandwiched configurations at 300 K in the ordered and disordered basins. We extended each simulation by 100 ns in order to get more equilibrated data. We generated simulated patterns using the extended of simulation trajectories. The patterns for all structures are shown and compared to experiment in Figure 8.

The simulated XRD patterns show moderate qualitative agreement with experiment. R-alkanes and R-pores appear in the expected location. R-pores is more intense than experiment, likely because we are simulating a near perfect, infinite hexagonal array. The real system has defects and domain misalignment which decreases the overall intensity. R-spots appears to be weaker, except for the ordered basin sandwiched configuration, in the simulated patterns. They are also partially engulfed by the wide R- $\pi$  reflection. R- $\pi$  appears

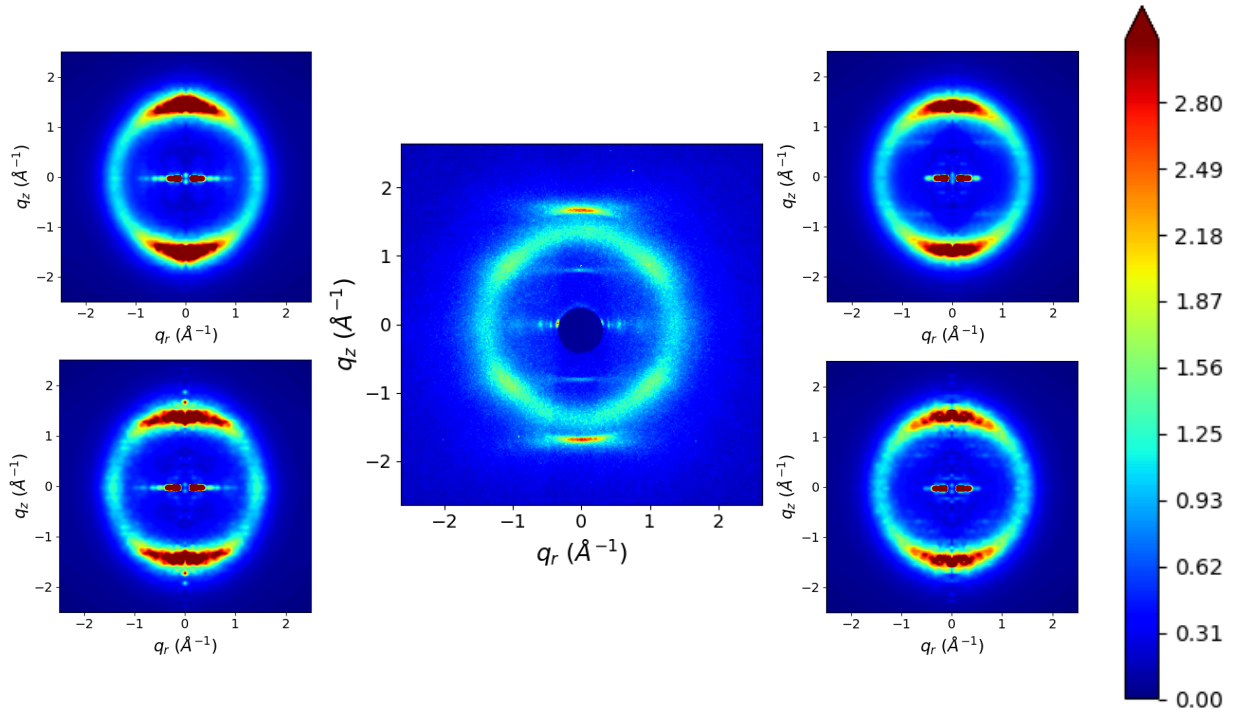


Figure 8: Simulated X-ray diffraction patterns show some qualitative agreement with experiment. Shown is a comparison of the (a) Sandwiched, ordered basin (b) Sandwiched, disordered basin (d) Parallel Displaced, ordered basin and (e) Parallel Displaced, disordered basin configurations with (c) experimental WAXS. Quantitative comparisons of the relative intensities of reflections of interest are present in Table 1. In all cases, R-double is not present.

at a lower  $q_z$  value than experiment. In all systems, the reflection reaches its maximum at  $q_z < 1.5 \text{\AA}^{-1}$  which means that monomers prefer to stack at least  $4.2 \text{\AA}$  apart rather than  $3.7 \text{\AA}$ . R-double does not appear in any of the patterns.

The simulated XRD patterns of the parallel displaced configurations show an additional reflection due to their helical structure. There are horizontal reflections near  $|q_z| = 0.7 \text{\AA}^{-1}$ , half of the  $q_z$  value of R- $\pi$ . The reflection does not cross through  $q_r = 0 \text{\AA}^{-1}$  so it does not appear for the same reason as R-double. This type of pattern is characteristic of a helix (reference something). It is possible that these reflections contribute to the continuation of R-double into R- alkanes, as seen in the experimental pattern.

We quantified the numerical discrepancies present when comparing the relative intensities of each reflection of interest between experimental and simulated patterns. Table 1 shows

the relative intensities of each reflection for all systems tested. The patterns are normalized so that the average intensity of R-alkanes must equal 1. We measured the approximate intensity of R- $\pi$  by measuring the intensity of the peak shown by the cross-section of the 2D pattern at  $q_r = 0$ . The relative intensity of R- $\pi$  is significantly higher than experiment in our simulations. R-spots is measured as the average intensity within the region bounded by a 'spot'. Spots are identified based on visual inspection. If the spots were not easily discernable, then the intensity was taken as that of the intersection of R-alkanes at half the  $q_z$  value of R- $\pi$ , since that is where it appears experimentally. The intensity of R-spots is slightly lower than experiment in all cases. There is no R-double intensity to be measured. Figures are provided in section S6 to make these measurements clear.

**Table 1: The simulated XRD patterns of the systems tested, normalized so that the average intensity of R-alkanes equals 1, show R- $\pi$  reflections that are significantly higher than experiment and R-spots reflections that are slightly lower than experiment. R-double does not appear in any patterns, and thus has no measurable intensity.**

| Reflection | Configuration |            |           |            |            |           |
|------------|---------------|------------|-----------|------------|------------|-----------|
|            | Experiment    | Sandwiched | Parallel  | Disordered | Disordered |           |
|            |               |            | Displaced | Sandwiched | Parallel   | Displaced |
| R-alkanes  | 1.0           | 1.0        | 1.0       | 1.0        |            | 1.0       |
| R-spots    | 1.3           | 1.3        | 1.2       | 1.1        |            | 1.2       |
| R- $\pi$   | 2.8           | 44.0       | 7.7       | 8.4        |            | 10.1      |
| R-double   | 0.9           | —          | —         | —          |            | —         |

The diffraction patterns show some noise, especially along the axis where  $q_r=0$ . This noise can be suppressed by sampling more uncorrelated equilibrium configurations (See section S7). Unfortunately, our simulations are not long enough to sample enough independent configurations. Increasing the number of trajectory frames used to simulate the structure factor within a given interval of time does not offer any improvement.

There are clear differences between simulated and experimental results that must be addressed and justified. We will explore the origin of each experimental reflection and form structural hypotheses related to their appearance in our simulated patterns. Specifically, we

want answer:

1. What is the origin of R-spots?
2. Why is the intensity of R- $\pi$  so much greater than experiment?
3. What is the origin of R-double?

### 3.2.1 Origin of R-spots

We observe an increase in the intensity of R-spots when we simulate systems at 280K. R-spots is most intense in the ordered basin sandwiched configuration (Figure 9b). The relative intensity of R-spots is higher than in experiment (1.5 vs. 1.3). R-double is still not present. We will use this configuration to more thoroughly explore the origin of R-spots.

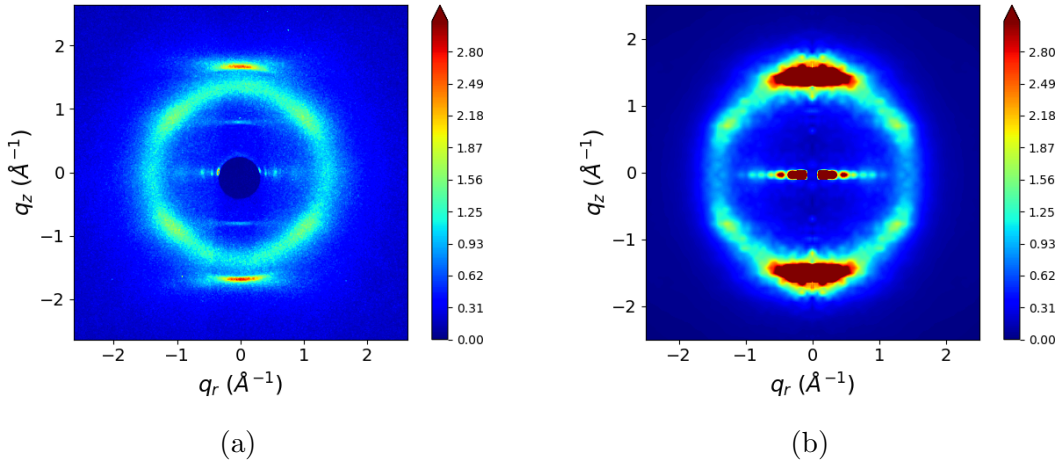


Figure 9: R-spots increases in intensity when the temperature of the system is lowered to 280K. In this case, the simulated R-spots is more intense than experiment.

The R-spots signal is not a result of alkane chain tilt. Previous literature has attributed the spots in this particular WAXS pattern as the product of tilted alkane chains.<sup>12</sup> We looked closer at the sandwiched configuration simulated at 280K. We measured the tilt angle of the alkane chains and showed that our system equilibrates to an average tilt angle of -2°(Fig. 10).

To understand the origin of R-spots, we determined which atoms gave rise to the feature. Since R-spots is present as higher intensity spots within R-alkanes, it is likely that the spots

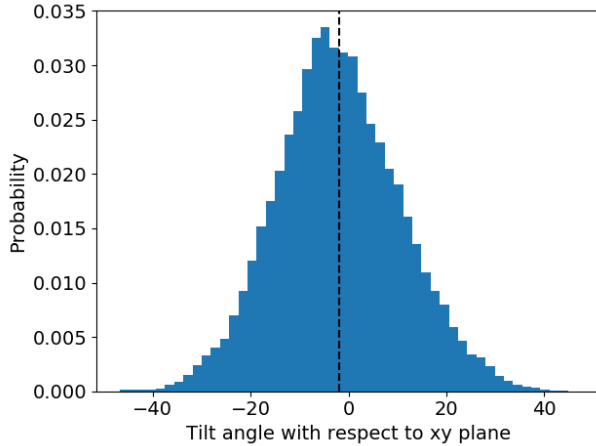


Figure 10: We measured the angle made between each monomer alkane tail and the membrane plane. The average tilt angle (dashed line) is near  $-2^\circ$  which is far from the  $37^\circ$  tilt angle previously used to explain R-spots.

arise as a consequence of the tails. By removing all non-tail atoms from the trajectory and simulating a diffraction pattern with the remaining atoms, we were able to isolate the cause of the spots to the tails (Figure 11). Since the tails stay nearly flat, we plotted the centroids of the tails (Figure S-17) and measured the angle between each centroid and its nearest neighbors with respect to the plane of the membrane. We see distinct peaks in the distribution of these angles (Figure 12).

The peaks in the nearest neighbor angle distribution are consistent with the location of R-spots. The peaks of interest in Figure 12a are located at  $\pm 33^\circ$  which is the same location where the highest intensity of spots are located on the simulated patterns. We confirmed this conclusion by radially integrating the 2D WAXS pattern for  $|\mathbf{q}|$  values between 1.4 and 1.57 (between 4 and 4.5 Å in real space). We observe distinct peaks ca.  $30^\circ$ , in close agreement with the previously measured angle distribution (Figure 12b). We performed the same integration on the raw experimental data and found the angle at which R-spots reaches its highest intensity to be  $\pm 37^\circ$  which is a reconcilable difference with our simulated results.

There are a couple reasons why we see stronger ordered chain packing at 280 K compared to experimental conditions of 300 K.

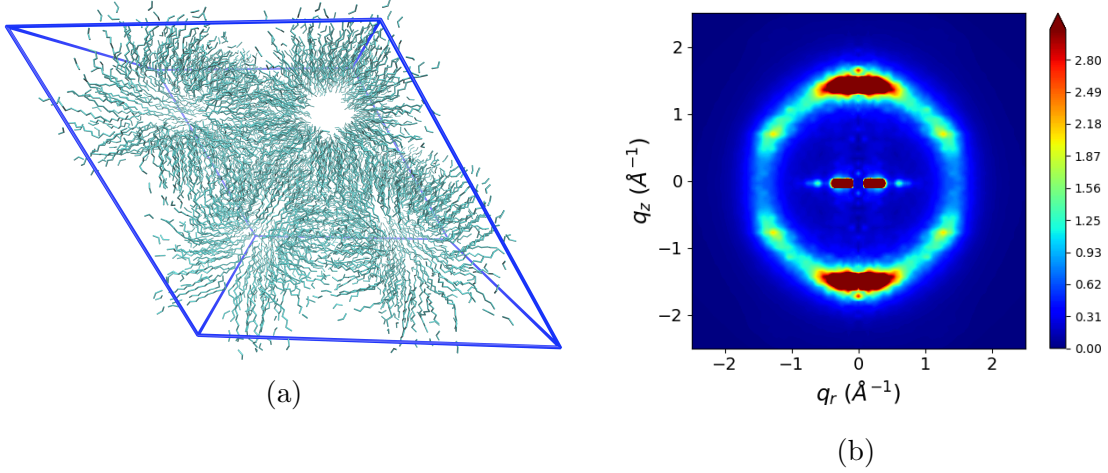


Figure 11: (a) We removed all atoms except carbon atoms that constitute the tails from a sandwiched configuration trajectory. (b) The simulated XRD pattern of the tail-only trajectory still shows R-spots

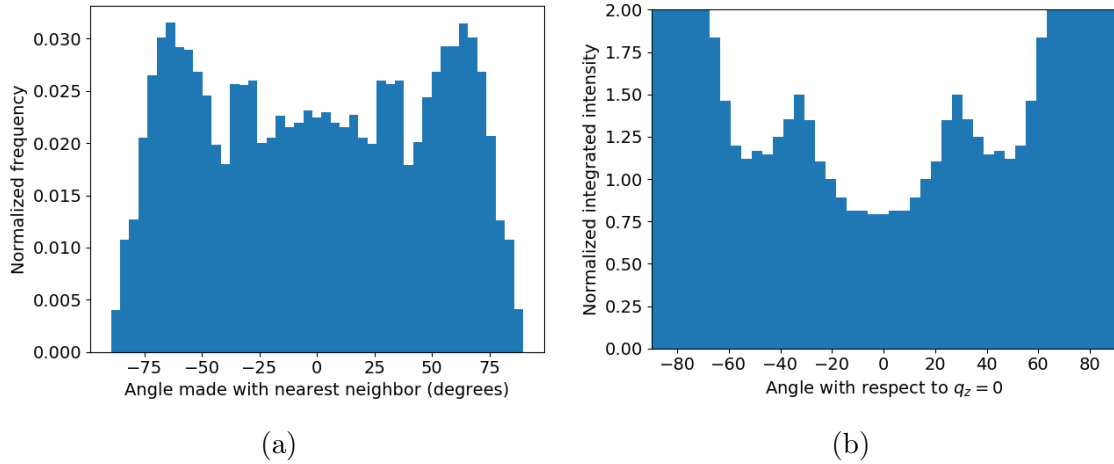


Figure 12: We hypothesize that R-spots is the result of ordered tail packing. Defining the membrane plane to be  $0^\circ$ , we measured the angles between each alkane chain tail centroid and its nearest neighbor centroids for the equilibrated sandwiched configuration simulated at 280K. Peaks that appear in each distribution are centered near  $\pm 33^\circ$ . We radially integrated the simulated XRD patterns of the parallel displaced and sandwiched configuration within the region bounding R-alkanes. Peaks appear in the same location as the angle distributions which corroborates our hypothesis.

1. The difference between 280 K and 300 K is relatively small. Our forcefield parameters may not correctly model the behavior of the tails at 300 K (citation?).
2. Monomers aren't as confined at 300 K in our simulations versus experiment. If the

head groups packed 3.7 Å apart, the tails would be more confined and forced to pack between vertically adjacent monomer tails. In our case, the tail region is less dense than experiment which gives the tails freedom to organize in a more entropically favored disordered state.

### 3.2.2 Discrepancies between R- $\pi$

We plotted the one-dimensional pair distribution function,  $g(z)$ , for the centers of mass of monomer phenyl rings (Figure 13). We used this information to understand how far apart monomers stack within monomer columns and the degree to which they are correlated.

**Table 2:** The correlation length is larger for systems in the ordered basin. The equilibrated vertical stacking distance,  $d_{equil}$ , is also smaller.

| System             | $d$ (Å) | $d_{equil}$ (Å) | Correlation Length (Å) |
|--------------------|---------|-----------------|------------------------|
| Sandwiched         | 3.7     | $4.27 \pm 0.03$ | $4.5 \pm 0.4$          |
| Parallel Displaced | 3.7     | $4.33 \pm 0.04$ | $15.5 \pm 1.9$         |
| Sandwiched         | 5.0     | $4.48 \pm 0.07$ | $3.2 \pm 0.9$          |
| Parallel Displaced | 5.0     | $4.60 \pm 0.08$ | $< d_{equil}$          |
| Experiment         | –       | 3.70            | $10 \pm 1$             |

Monomers in the ordered basin stack closer together than those in the disordered basin (Table 2). We calculated the equilibrated vertical distance,  $d_{equil}$ , between monomers using Equation 3. Monomers in the ordered basin stack ca. 0.2 and 0.3 Å closer than those built in the disordered basin in the sandwiched and parallel displaced configurations respectively. The distance between stacked monomers is greater than experiment by 0.5 - 0.9 Å across all cases. This behavior is not surprising since GAFF models atoms as point charges and does not appropriately model the aromatic  $\pi - \pi$  interactions which would cause the monomers to stack closer together. Ordered basin systems are likely the best choice for transport studies.

The correlation length between stacked monomer head groups of the ordered systems also show closer agreement with experiment (Table 2). We calculated the correlation length of each system using Equation 2. We could not extract a reliable correlation length from the

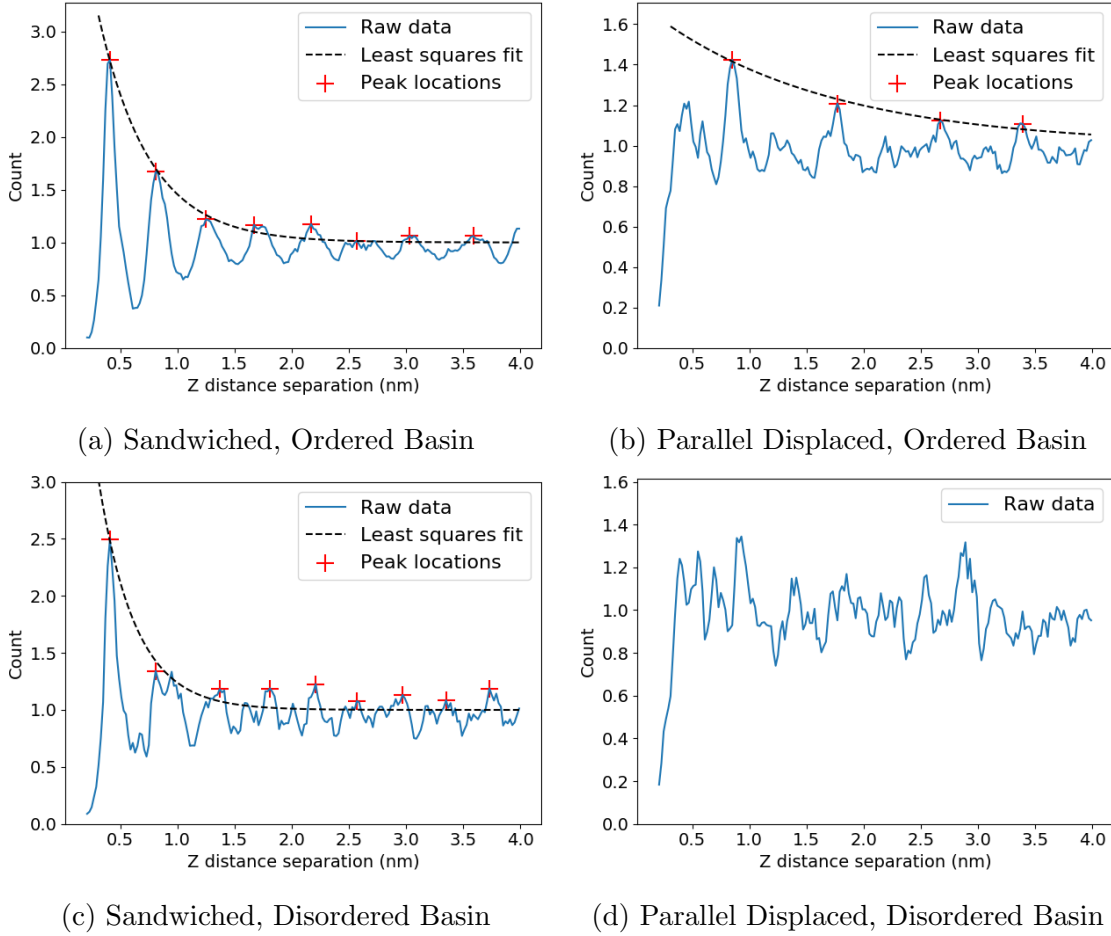


Figure 13: 1D correlation functions of the center of masses of aromatic head groups,  $g(z)$ , show decaying oscillatory behavior. We calculated the correlation length by fitting a decaying exponential function (Equation 2) to the peaks of  $g(z)$ . The correlation length is longer for ordered basin systems (Table 2). We did not attempt to calculate the correlation length for (d) because there are no clear peaks. We assume that its correlation is less than the vertical distance between monomers.

disordered parallel displaced configuration. The amount of noise in the correlation function and the lack of an initial peak suggests that the correlation length is less than  $d_{equil}$ . In general, we see that correlation length increases as monomers stack closer together. The same trend has been seen in molecular dynamics studies of polymer fluids.<sup>7</sup> We hypothesize that the correlation length of the sandwiched configuration would increase to a value near experiment if monomers packed closer together.

The persistent oscillatory behavior of the correlation function may in part explain the high intensity of R- $\pi$  relative to experiment. The way we calculate correlation length is unique to the rate of decay of  $g(z)$  but not its exact shape.  $g(z)$  for our simulated systems, especially the sandwiched configurations, shows peaks which persist across the entire correlation function. If the peaks at large values of z instead decay to 1 uniformly, the correlation length could remain nearly the same, but R- $\pi$  would have a reduced intensity. The monomer head groups in our simulations do not move enough to create the noise which would cause such behavior. See Section S9.1 of the supporting information for illustrative examples.

The system size does not significantly alter the intensity of R- $\pi$ . We equilibrated a sandwiched system with twice as many monomers per column so that the system size doubled in the z-direction. The correlation length increases modestly from  $4.5 \pm 0.4$  to  $7.3 \pm 1.2$  Å, and the intensity of R- $\pi$  decreases from 44.0 to 39.4. Visually, the correlation functions are nearly identical (See Figure ??).

The simulated intensity of R- $\pi$  is also more intense than experiment because our system models near-perfectly straight pores with no defects. Nearly all of the intensity in R- $\pi$  of our simulated patterns is concentrated at a single point. Figure 14a shows the simulated pattern of the ordered sandwiched configuration with the upper boundary on the colorbar adjusted to be 6x higher than those shown in Figure 8. The only distinguishable reflections are those of R- $\pi$  and R-pores. In the experimental pattern (Figure 14b, the intensity is more evenly spread out over all of R- $\pi$ .

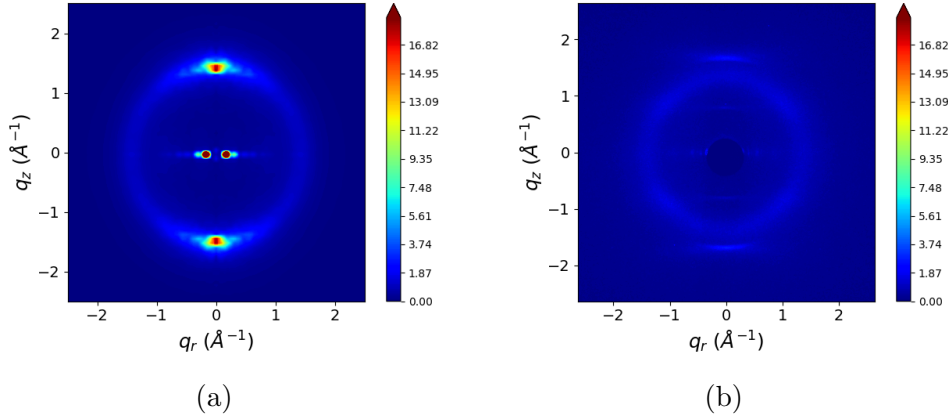


Figure 14: R- $\pi$  and R-pores are far more intense than the other major reflections in simulated diffraction patterns (a). Here, the colorbar was scaled so that the max is 6x higher than all other plots.

### 3.2.3 Origin of R-double

There is no way to produce R-double without a more complex initial configuration. We calculated the structure factor of simple systems that mimic the parallel displaced and sandwiched configurations. Neither give rise to R-double. (See Figure "fourier transforms of simple systems" in supporting info). The appearance of R-double implies a vertical modulation in electron density every 7.4 Å. It is possible that this modulation occurs in either the head or the tails. There is not a unique solution to this problem, however we can speculate based on what makes the most physical sense.

We can produce R-double if our initial configuration contains alternating parallel and antiparallel carboxylate groups relative to the plane of the monomer's phenyl ring. (Figure 15a). It is difficult to physically justify this system. Systems built this way are only stable if position restraints are placed on all head group heavy atoms. Carboxylate groups quickly revert to the parallel position as restraints are released. There is an appreciable energy barrier that prevents rotation of carboxylate groups attached to phenyl rings since the group extends the system's  $\pi$  conjugation. (citation) (See figure in supporting info with energy barrier plots) There are instances where carboxylate groups in other systems rotate out of plane. Bushey et al. showed that bulky carbonyl-containing substituents of stacked arene

molecules tended to tilt  $45^\circ$  in order to relieve steric strain, thus allowing  $\pi$ - $\pi$  stacking between molecules, and to hydrogen bond with neighboring molecules. Lorenzo and Graña found 3 stable dimers of gallic acid (from which the monomer, Na-GA3C11 is derived) with adenine. In all cases, the carboxylate group remained planar, even with evidence of hydrogen bonding between the carboxyl group and nitrogen atoms of adenine. The monomers which we are studying have no opportunities to hydrogen bond and are confined so that any rotation about the phenyl– carboxylate bond would be sterically hindered.

We can also produce R-double if layers are not uniformly spaced. Rather, monomers might form pairs that stack less than  $3.7\text{ \AA}$  apart, and whose center of masses are spaced  $7.4\text{ \AA}$  from the next pair of monomers (Figure 15b). To our knowledge, there have been no studies that specifically address the possibility of a configuration like this. Our forcefield causes our system to tend towards uniformly spaced layers. As expected, simulations of this type of system are only stable if position restraints are applied to heavy atoms of the phenyl rings.

Our final hypothesized configuration which produces R-double focuses on the orientation of the tails. In this configuration, monomers are rotated so that the vector created by the bond extending from the carboxylate carbon to the phenyl ring is oriented  $\pm 15^\circ$  with respect to the vector extending from the carboxylate carbon to the pore center (Figure 15c). Every other monomer layer is rotated  $+15^\circ$  and those in between are rotated  $-15^\circ$ . This configuration allows monomer tails to sit between adjacent monomer tails which may be the most favorable way for them to pack. This configuration is stable short-term while unrestrained however R-double quickly fades after a few nanoseconds of simulation. Still, this may be the most reasonable explanation for the appearance of R-double. The long-term stability of a configuration similar to this may be feasible if monomers stay stacked  $3.7\text{ \AA}$  apart.

### 3.3 Slow dynamics

We observe unusually slow dynamics in our system relative to other liquid crystal systems. Typical diffusion constants for columnar liquid crystals have been reported to be on the order of  $10^{-11} \text{ m}^2/\text{s}$ .<sup>36</sup> We measured the diffusion constants of monomers in each of the systems we studied (See Table S-2) and learned that they are all on the order of  $10^{-14} \text{ m}^2/\text{s}$ . Our systems may be frozen in a glassy state. It is also possible that we are simply observing characteristics of the experimental system. There has been no experimental work done to study diffusion of Na-GA3C11 monomers in the Col<sub>h</sub> system and no measurement of the glass transition temperature. Such a low diffusion constant is not unheard of. A more recent study reported a diffusion constant of  $1.2 \times 10^{-14} \text{ m}^2/\text{s}$  for a different liquid crystal that formed a hexagonal columnar phase.<sup>37</sup>

There is not enough movement on the timescales we simulated for the system to consistently reach a structure equivalent to experiment. In all cases our monomers equilibrate to a stacking distance that is too large compared to experiment. While this may be in large part due to the forcefield's inability to model aromatic interactions, it is also possible that the monomer tails do not pack as tightly as they could. More densely packed tails could allow the monomers to stack closer together.

We quantified the movement of the tails during our simulations by calculating the autocorrelation function of the dihedral angle formed around the bond between the head groups and the ether oxygens which attach the tails to the head group (See Figure S3). We exclude the dihedral from the middle tail since it is fundamentally different than the two symmetric outside tails. We limited these studies to the sandwiched configuration for simplicity.

The ether dihedrals become decorrelated on a reasonable timescale when the temperature is raised. At 300K (Figure 16a), the autocorrelation function does not cross the x-axis until  $\approx 105 \text{ ns}$  meaning that tails might only fully rotate 4 times over the course of the 400 ns that we studied. Additionally, the correlation function plateaus near a value of -0.2 which indicates that the tails are starting in an unfavorable configuration. We implemented distance

restraints between the centers of mass of monomer head groups to preserve the hexagonal phase, then rose the temperature of the equilibrated 300 K ordered basin sandwiched system to 500 K. We witnessed decorrelation of ether dihedrals after  $\approx$  11 ns with a plateau at 0, (Figure 16b) indicating a complete loss of memory. We annealed the resultant configuration back down to 300 K over 200 ns to see if the increased rotational freedom might allow the system to relax into to a more tightly packed configuration.

Decorrelating the ether dihedrals at high temperature, followed by thermal annealing does not improve packing in our model. In the ideal case, if all monomers stacked 3.7 Å apart, the z-dimension of our unit cell should be 7.4 nm. In the ordered basin, sandwiched system studied in this paper, the z-dimension of the unit cell equilibrated to 8.87 nm, which is roughly consistent with the stacking distance reported in Table 2. After 200 ns of annealing from 500K to 300K, the z-dimension of the unit cell was 9.22 nm. We repeated the annealing procedure over the course of 400 ns and the final z-dimension of the unit cell was 9.20 nm. Much longer annealing simulations may get the system to the correct density, but we do not have the resources to further explore this approach.

### 3.4 Chemical composition of pore columns

We are most interested in the composition of the pores since we would like to study transport mechanisms within them. We have shown that the tails possess a certain degree of order which is necessary in order to create the complex WAXS pattern shown experimentally, but they will not be involved in a separation process. We aim to further understand the pore architecture and observe the differences, if any, between the different equilibrated configurations studied so far.

We plotted the number densities of heavy atoms in the head group, carbon atoms in the tail region and all sodium ions (Figure 17). For the head group region, we used heavy atoms making up the aromatic rings and carboxylate groups. For the tail region we used carbon atoms of the monomer tails (See Figure S2 for a diagram). We averaged the histograms over

at least 50 ns of equilibrated trajectory.

There is a partition between the hydrophobic and hydrophilic regions, however it is a gradient in composition, rather than an abrupt division. The system does not confine sodium ions and head groups to just within the pore region. Based on size-exclusion experiments, we define the pore radius to be 0.6 nm.<sup>7</sup> We see in all cases, that 19% of sodium ions exist outside the pore region (except sandwiched, ordered basin, where 16% are outside the pore). Additionally, we see that in all cases, about 3% of the plotted tail density is located within the pore region (except ordered sandwiched, where 1.5% are within the pore region). These observations bring into question how one should define a pore in these types of systems. One usually measures a membrane's pore radius based on the size of a molecule it can reject, however it is not clear where the edges of the pores are and what size molecule would fit through. We leave these investigations for a future study.

In all cases, the space in the pore region is filled with a mixture of sodium ions and head groups. The ordered parallel displaced configuration has the highest density of sodium ions at the pore centers. Both the ordered and disordered parallel displaced configurations have higher concentrations of head groups in the center. This observation highlights that the pore region is dense, not hollow, and may impede transport of solvent and solutes. We observe how this changes when water is added to the system.

In general, the composition of each region, particularly the pore region, is similar between all systems. We believe we can study transport in any of the systems presented here and extract similar transport mechanisms. We will need to verify that this assumption is true.

### 3.5 Effect of Water on Structure

We explored the effect of water on pore structure, addressing question (4), by preparing parallel displaced and sandwiched configurations according to the wet equilibration procedure. We limit the discussion to the ordered pore basin since it produces equilibrated configurations closest to experiment. There is no experimental measurement of trace water concentration in

these membranes so we tested a range of water concentrations from 1 to 5 percent. Figure 18 shows the simulated diffraction patterns resulting from each configuration.

In all cases, water disrupts structuring of the model. When we add water to the system, the intensity of the reflections decrease. In systems built with 5 wt% water, R- $\pi$  and R-spots become nearly indistinguishable from R-alkanes. In systems built with 5 wt% water, the pore region becomes filled with water. We plotted the number density of components in this system. As with the dry systems, we see a gradual compositional transition from hydrophilic to hydrophobic. We see that the pores become a mixture of water molecules and sodium ions (Fig. 19). We also see that water exists in the tail region which may decrease the tail ordering and explain the decrease in intensity of R-spots.

The membrane swells when we introduce water. The location of maximum head group density shifts from 0.35 to 0.62 nm and from 0.44 to 0.61 nm in the parallel displaced and sandwiched configurations respectively. Again, we observe the existence of ions, head groups and water outside the pore region, however in the hydrated system, the head groups drift beyond 1.5 nm from the pore center. In the dry systems, head groups did not wander beyond 1.4 nm from the pore center. Both observations suggest that water pushes all components radially outward from the pore center, characteristic of a swelling process. The plots of  $g(x, y)$  for dry and wet systems are compared in Figure 20. They further illustrate how the system swells in the presence of water. This system is a closer representation of the H<sub>II</sub> phase which is typically synthesized with ca. 8 wt% water. Further investigation of hydrated systems can help unravel the mechanisms for selective transport in separations of aqueous solutions.

Water is not necessary to maintain an ordered pore structure. We do not eliminate the possibility that water is necessary in order to drive self-assembly, but studying the mechanisms of self-assembly is beyond the scope of this work. According to our model, once the system has formed the Col<sub>h</sub> phase, adding water only drives disorder of the pore structure. In the true equilibrium configuration, if water exists, it is primarily confined to

the pore region where there is no driving force for aggregation of water molecules. In the case of trace water, water molecules will be too sparse to form a hydrogen bonding network.

### 3.6 Model Ionic Conductivity Measurements

We used equilibrated systems in the ordered pore basin to calculate ionic conductivity since we believe their structures are the closest match to experiment. Our models give reasonable estimates of ionic conductivity when compared to experiment. We compare calculated values of ionic conductivity obtained using the Nernst-Einstein relation and Collective Diffusion model in Figure 21. The two methods agree with each other within error, although the uncertainty obtained using the Collective Diffusion model is much higher. We require much longer simulations to lower the uncertainty, however it is not feasible to do so with a large system. We will only use the Nernst-Einstein relation in future calculations of this type.

The calculated values of ionic conductivity are higher than experiment by an order of magnitude. One can justify the reason for this result by considering the real system studied experimentally. The ionic conductivity measurement to which we are comparing was done with a 80  $\mu\text{m}$  thick film, nearly 10,000 times thicker than our simulated system. The thick film is likely imperfectly aligned and has defects leading to non-contiguous pores. It has been shown that there is a large dependence of ionic conductivity on the alignment of the pores. The ionic conductivity of an isotropically aligned film is ca. 85 times lower than that of a nearly aligned film referenced here.<sup>12</sup> We hypothesize that a thin, perfectly aligned film would have a value of ionic conductivity in closer agreement with our model.

### 3.7 Effect of Crosslinking

We applied our crosslinking algorithm to equilibrated sandwiched and parallel displaced configurations in the ordered pore basin. We allowed the crosslinking algorithm to propagate until greater than 90 % of vinyl groups were either involved in a crosslinking reaction or were terminated. See section S10 for further details on the crosslinking algorithm. We allowed

the crosslinked configurations to simulate for 100 ns further in the NPT ensemble.

There are minor changes to the physical characteristics of these systems when they are crosslinked (See Figure 22). The ionic conductivity of the sandwiched configuration decreases while that of the parallel displaced configuration stays the same. The pore spacing decreases in both systems by 0.07 nm. The vertical monomer stacking distance increases in the sandwiched configuration and decreases in the parallel displaced configuration, however the values of crosslinked configurations fall within uncertainty of their un-crosslinked counterparts. The correlation length decreases in both systems, but is most pronounced in the parallel displaced system.

## 4 Conclusion

We have used a detailed molecular model of the Col<sub>h</sub> phase formed by Na-GA3C11 in order to study its nanoscopic structure. While there have been efforts to model formation of various liquid crystalline phases with molecular dynamics, to our knowledge there have been no studies which attempt to examine their structure with the same level of detail presented here.

We observed a number of metastable configurations, stable for hundreds of nanoseconds, which do not fit the experimental profile we have tried to match. We explored two classes of metastable basins which are dependent on the initial vertical stacking distance between monomers : the ordered and disordered pore basins. We expect that these metastable configurations will eventually rearrange and converge to a single equilibrium structure. We conducted extensive analysis in order to isolate structures which most closely resembles the true equilibrium structure.

The system's pore spacing is most consistent with experiment when systems are built with 5 columns per pore. The distance between pores increases with the number of columns per pore. Pores pack closer together in the disordered pore basin. Systems built with 6

columns per pore in the disordered basin expand in the z-direction which suggest that it may rearrange to 5 columns per pore long term.

We have maximized our model's consistency with the experimental WAXS pattern. We show that R-alkanes and R-pores appear where expected. We learned that R-spots is likely due to ordered alkane chain packing. R- $\pi$  appears at lower q values than experiment because monomer stack too far apart. We found that our model cannot reproduce R-double, however we have come up with a three different mechanisms that lead to the reflection's appearance. The most likely explanation is that monomers within each column rotate ca. 15° with respect to their vertically adjacent neighbors so that tails can pack together more tightly.

We characterized the environment centered around the membrane pores and learned that the pores are generally filled with monomer head groups and sodium ions. All systems studied showed a similar distribution of sodium, head groups and tails, which means we can study solute transport in any of the systems here and extract similar transport mechanisms. We also observed that there is not a hard partition between hydrophobic and hydrophilic regions, rather there is a gradient. This finding has raised questions about the nature of size-exclusion separations.

We learned that we do not need water to create well-defined pore structures. Systems whose pores were filled with varying amounts of water showed a decrease in structuring relative to dry systems. At higher water concentrations, the pores begin to swell, which may be more conducive to transport.

We justified that our system can reasonably estimate ionic conductivity. Our calculations are about 1 order of magnitude higher than experiment, however that is to be expected since we are simulating a perfectly straight and defect-free membrane.

Finally, we verified that our conclusions do not change when the system is cross-linked by the algorithm we implemented. The diffraction pattern weakens relative to the uncross-linked system, the ionic conductivity drops by a factor of ca. 1.5, in closer agreement with experiment, the pore spacing decreases and the membrane becomes thicker.

With the structural understanding gained by these simulations, we will evaluate transport of various solutes within the system. We will apply the knowledge gained from this study in order to suggest improvements to the existing system as well as to evaluate new unsynthesized LLC systems.

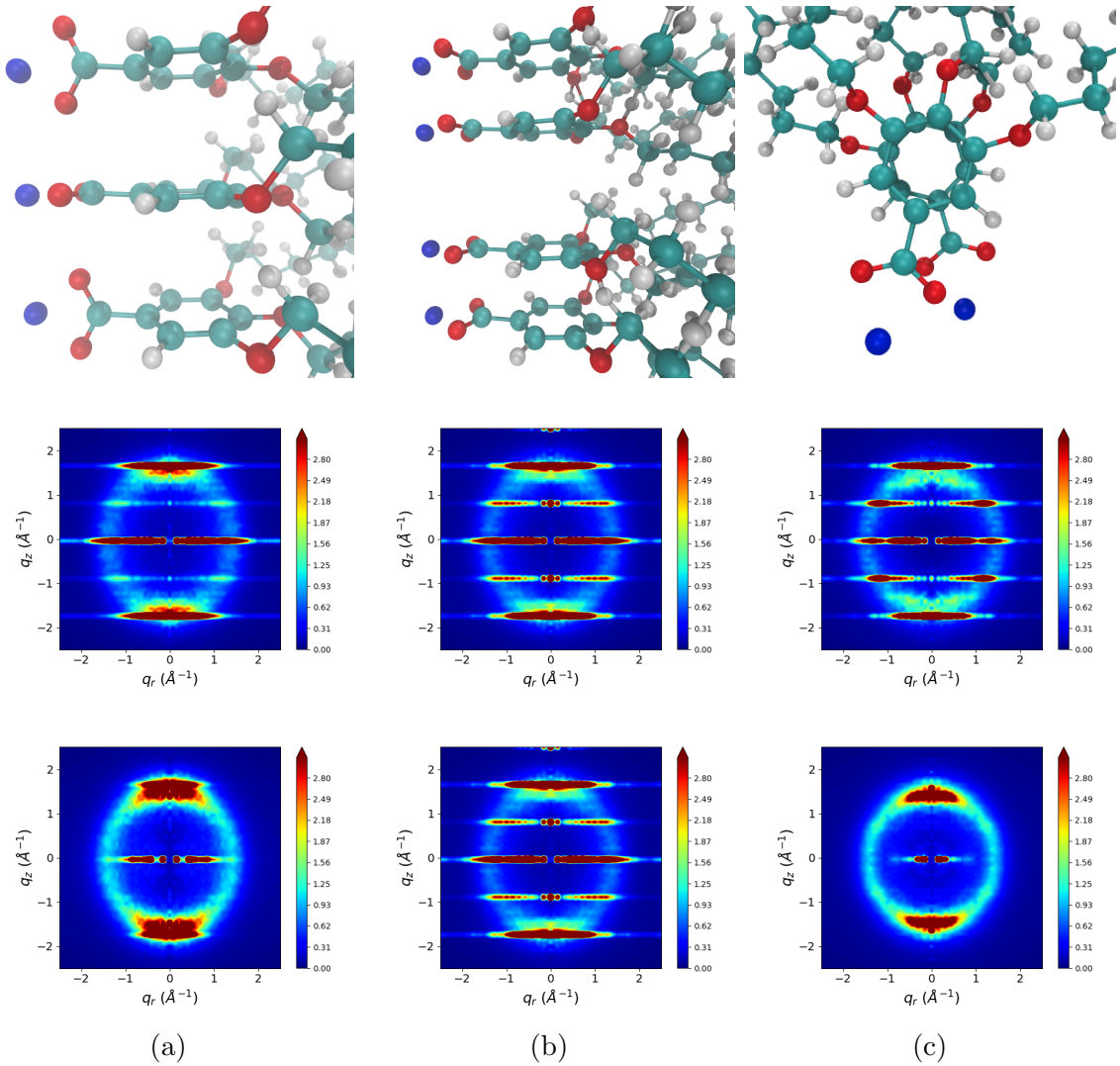


Figure 15: R-double is present in all three initial configurations tested while the heavy atoms in the headgroup are held in place with position restraints. R-double fades once the position restraints are released.

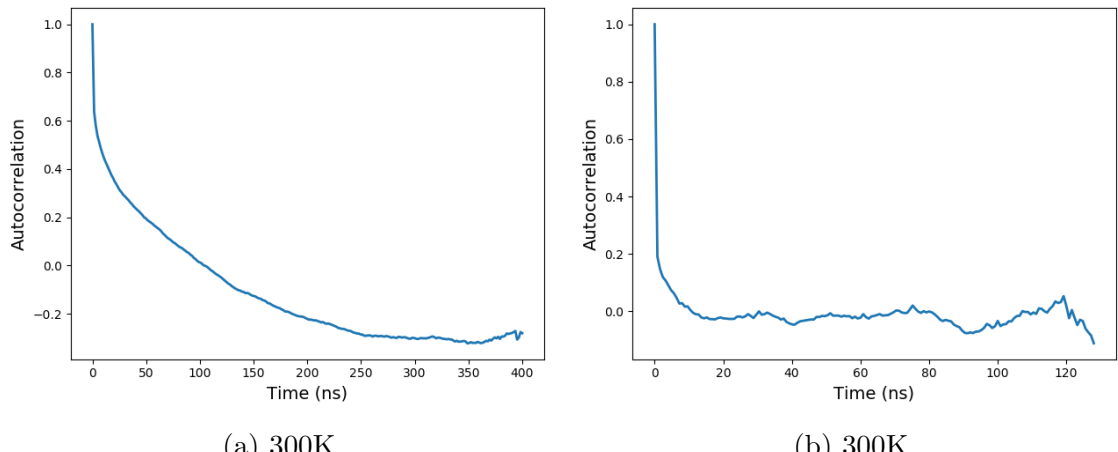
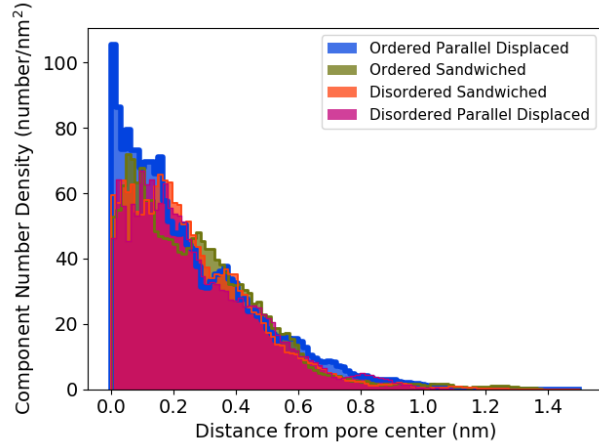
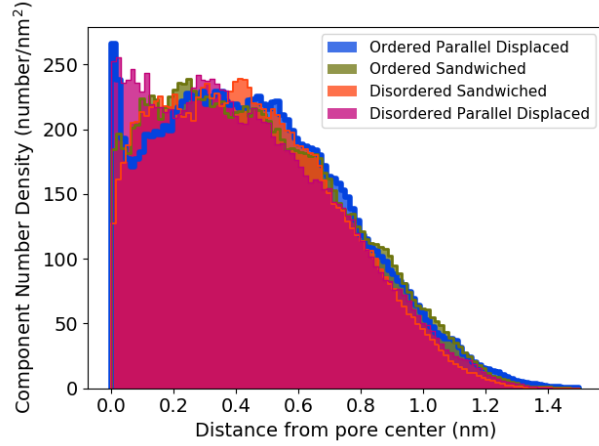


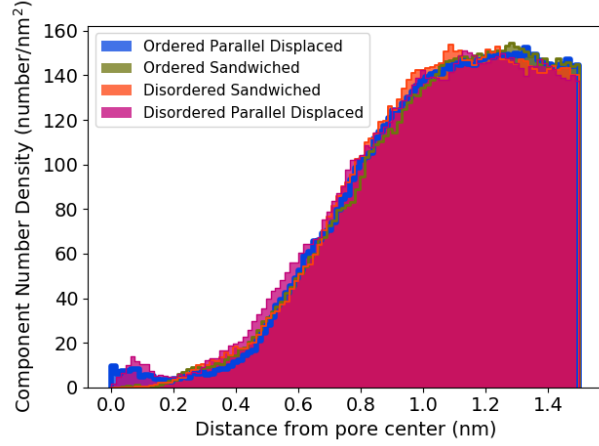
Figure 16



(a) Sodium Ions



(b) Head Groups



(c) Tails

Figure 17: In all cases, the component radial distribution functions exhibit a composition gradient transitioning from the hydrophilic to the hydrophobic regions. Systems with layers initially spaced 3.7 Å apart in the parallel displaced (a), and sandwiched (b) configurations both show the highest concentrations of ions and head groups away from the pore center. Systems with layers initially spaced 5 Å apart (c) and (d), both show the highest concentrations of ions and head groups near the pore center, implying a more uniform, disordered pore.

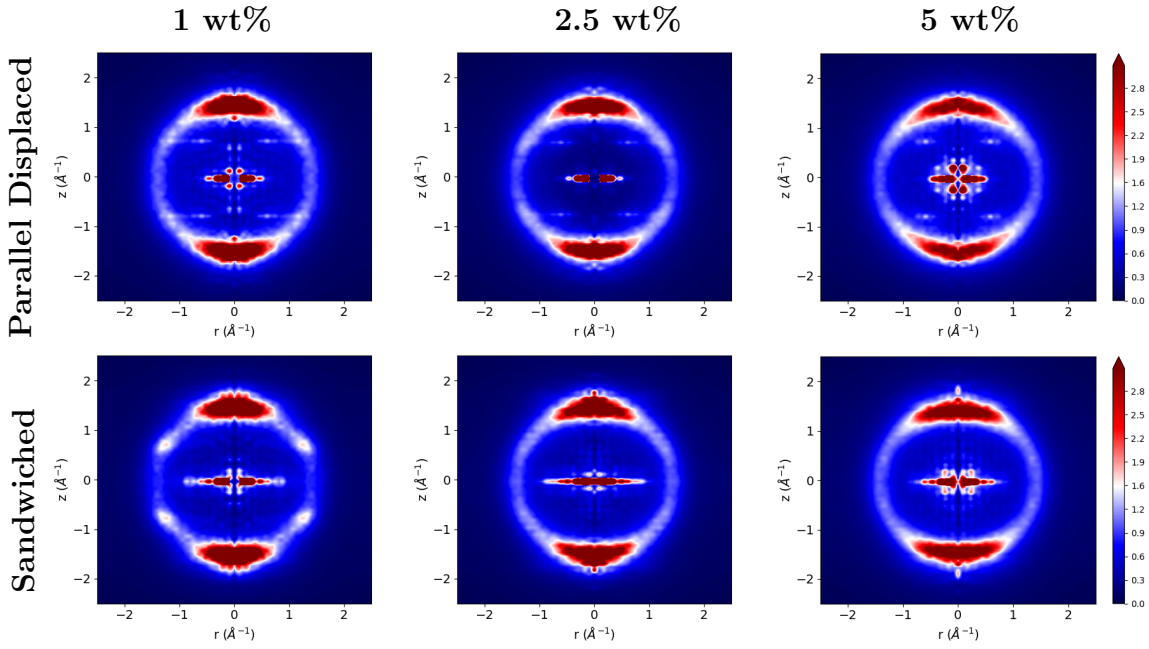


Figure 18: Simulated XRD patterns indicate that systems with added water are not as structured as the dry systems. As increasing amounts of water are added to both systems,  $R-\pi$  fades. When 2.5 wt% water is added to the sandwiched system,  $R-\pi$  gains back some intensity, but its magnitude is not greater than the dry system.  $R$ -spots also disappears as water is added. It is absent in all parallel displaced simulations, but fades gradually as water is added to the sandwiched configuration.

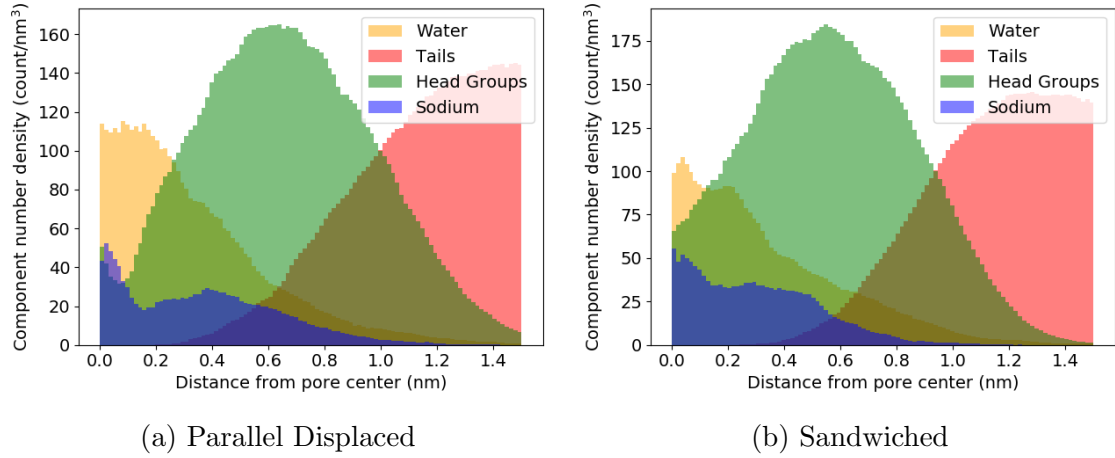


Figure 19: Water fills the membrane pores in the parallel displaced (a) and sandwiched (b) configurations. Head groups in the sandwiched configuration sit closer to the pore center than they do in the parallel displaced configuration. Both systems are composed primarily of water close to the pore center.

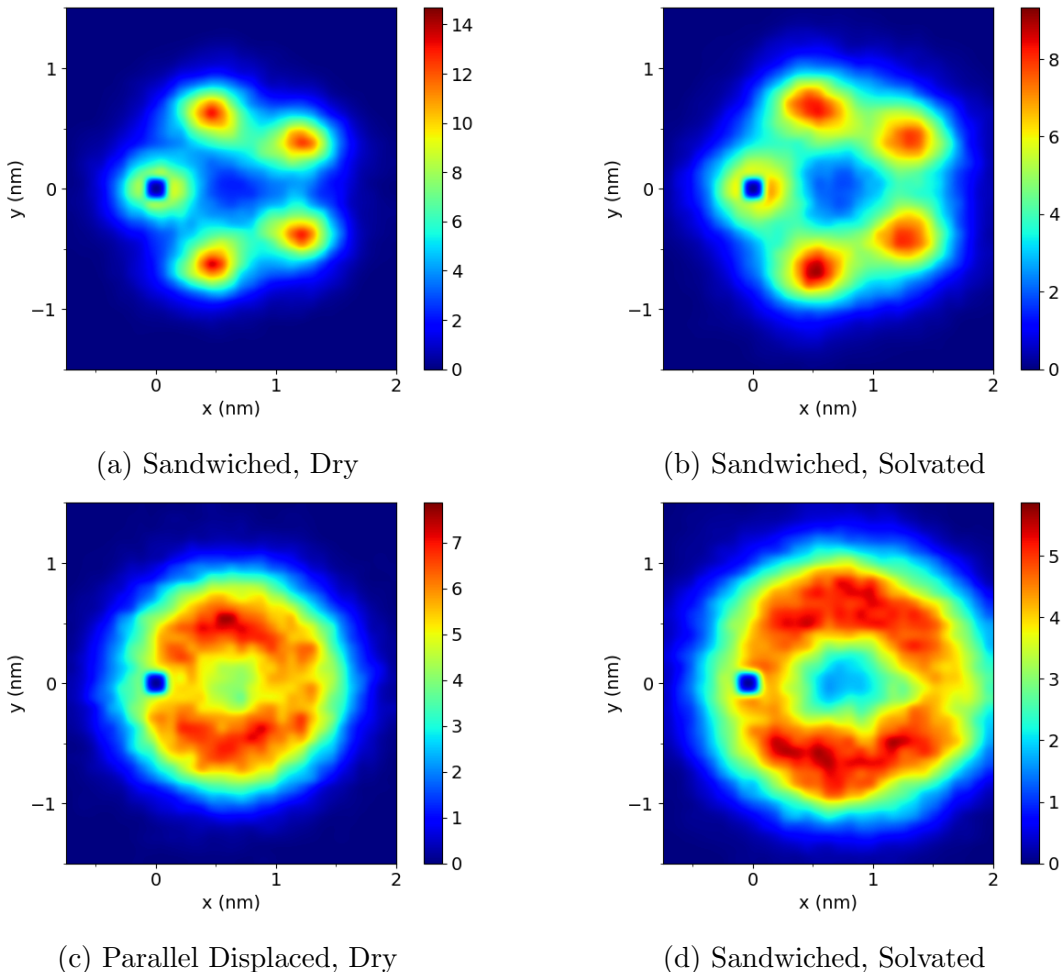


Figure 20:  $g(x, y)$  of monomer head groups illustrates how the pores swell in the presence of water.

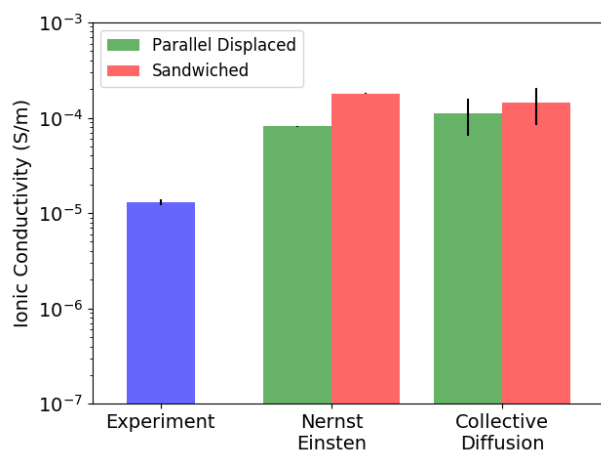


Figure 21: The Collective Diffusion model and the nernst-einstein relation yield agreeing values of ionic conductivity for both systems simulated. Both methods estimate the value of the ionic conductivity to be an order of magnitude higher than the experimental value.

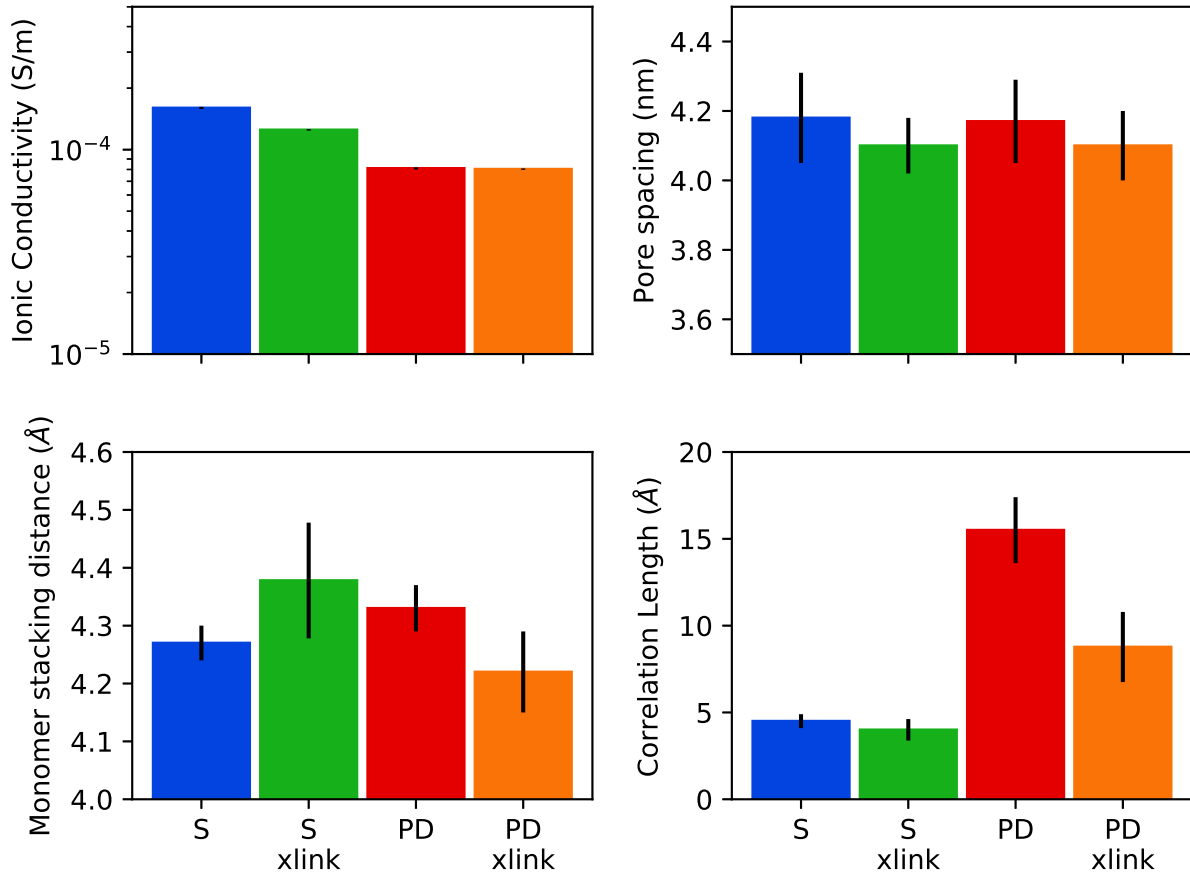


Figure 22: There are minor differences between the physical properties of a crosslinked (xlink) system versus an uncrosslinked system. The sandwiched configuration (S) exhibits a smaller decrease in its ionic conductivity, while the parallel displaced (PD) configuration remains constant. The pore spacing of both systems decreases upon crosslinking. The vertical distance between stacked monomers increases in the sandwiched configuration and decreases in the parallel displaced configuration. The correlation length decreases in both configurations.

## References

- (1) Dischinger, S. M.; Rosenblum, J.; Noble, R. D.; Gin, D. L.; Linden, K. G. Application of a lyotropic liquid crystal nanofiltration membrane for hydraulic fracturing flowback water: Selectivity and implications for treatment. *Journal of Membrane Science* **2017**, *543*, 319–327.
- (2) Theodori, G. L.; Luloff, A.; Willits, F. K.; Burnett, D. B. Hydraulic fracturing and the management, disposal, and reuse of frac flowback waters: Views from the public in the Marcellus Shale. *Energy Research & Social Science* **2014**, *2*, 66–74.
- (3) Werber, J. R.; Osuji, C. O.; Elimelech, M. Materials for next-generation desalination and water purification membranes. *Nature Reviews Materials* **2016**, *1*, 16018.
- (4) Gin, D. L.; Bara, J. E.; Noble, R. D.; Elliot, B. J. Polymerized Lyotropic Liquid Crystal Assemblies for Membrane Applications. *Macromolecular Rapid Communications* **2008**, *29*, 367–389.
- (5) Wijmans, J. G.; Baker, R. W. The solution-diffusion model: a review. *Journal of Membrane Science* **1995**, *107*, 1–21.
- (6) Smith, R. C.; Fischer, W. M.; Gin, D. L. Ordered Poly(p-phenylenevinylene) Matrix Nanocomposites via Lyotropic Liquid-Crystalline Monomers. *Journal of the American Chemical Society* **1997**, *119*, 4092–4093.
- (7) Zhou, M.; Kidd, T. J.; Noble, R. D.; Gin, D. L. Supported Lyotropic Liquid-Crystal Polymer Membranes: Promising Materials for Molecular-Size-Selective Aqueous Nanofiltration. *Adv. Mater.* **2005**, *17*, 1850–1853.
- (8) Donnan, F. G. Theory of membrane equilibria and membrane potentials in the presence of non-dialysing electrolytes. A contribution to physical-chemical physiology. *Journal of Membrane Science* **1995**, *100*, 45–55.

- (9) Hatakeyama, E. S.; Gabriel, C. J.; Wiesnauer, B. R.; Lohr, J. L.; Zhou, M.; Noble, R. D.; Gin, D. L. Water filtration performance of a lyotropic liquid crystal polymer membrane with uniform, sub-1-nm pores. *Journal of Membrane Science* **2011**, *366*, 62–72.
- (10) Hatakeyama, E. S.; Wiesnauer, B. R.; Gabriel, C. J.; Noble, R. D.; Gin, D. L. Nanoporous, Bicontinuous Cubic Lyotropic Liquid Crystal Networks via Polymerizable Gemini Ammonium Surfactants. *Chem. Mater.* **2010**, *22*, 4525–4527.
- (11) Carter, B. M.; Wiesnauer, B. R.; Hatakeyama, E. S.; Barton, J. L.; Noble, R. D.; Gin, D. L. Glycerol-Based Bicontinuous Cubic Lyotropic Liquid Crystal Monomer System for the Fabrication of Thin-Film Membranes with Uniform Nanopores. *Chem. Mater.* **2012**, *24*, 4005–4007.
- (12) Feng, X.; Tousley, M. E.; Cowan, M. G.; Wiesnauer, B. R.; Nejati, S.; Choo, Y.; Noble, R. D.; Elimelech, M.; Gin, D. L.; Osuji, C. O. Scalable Fabrication of Polymer Membranes with Vertically Aligned 1 nm Pores by Magnetic Field Directed Self-Assembly. *ACS Nano* **2014**, *8*, 11977–11986.
- (13) Matyka, M.; Khalili, A.; Koza, Z. Tortuosity-porosity relation in porous media flow. *Phys. Rev. E* **2008**, *78*, 026306.
- (14) Feng, X.; Nejati, S.; Cowan, M. G.; Tousley, M. E.; Wiesnauer, B. R.; Noble, R. D.; Elimelech, M.; Gin, D. L.; Osuji, C. O. Thin Polymer Films with Continuous Vertically Aligned 1 nm Pores Fabricated by Soft Confinement. *ACS Nano* **2016**, *10*, 150–158.
- (15) Resel, R.; Leising, G.; Markart, P.; Kriechbaum, M.; Smith, R.; Gin, D. Structural properties of polymerised lyotropic liquid crystals phases of 3,4,5-tris(\$mega\$-acryloxyalkoxy)benzoate salts. *Macromolecular Chemistry and Physics* **2000**, *201*, 1128–1133.

- (16) McIntosh, T. J.; Simon, S. A.; MacDonald, R. C. The organization of n-alkanes in lipid bilayers. *Biochimica et Biophysica Acta (BBA) - Biomembranes* **1980**, *597*, 445–463.
- (17) Govind, A. S.; Madhusudana, N. V. A simple molecular theory of smectic-C liquid crystals. *EPL* **2001**, *55*, 505.
- (18) Zhu, X.; Scherbina, M.; Bakirov, A.; Gorzolnik, B.; Chvalun, S.; Beginn, U.; Moller, M. Methacrylated Self-Organizing 2,3,4-Tris(alkoxy)benzenesulfonate: A New Concept Toward Ion-Selective Membranes. *Chem. Mater.* **2006**, *18*, 4667–4673.
- (19) Chaikin, P.; Lubensky, T. *Principles of condensed matter physics*, 1st ed.; Cambridge University Press, 1995.
- (20) Wang, J.; Wolf, R. M.; Caldwell, J. W.; Kollman, P. A.; Case, D. A. Development and testing of a general amber force field. *J. Comput. Chem.* **2004**, *25*, 1157–1174.
- (21) Wang, J.; Wang, W.; Kollman, P. A.; Case, D. A. Automatic atom type and bond type perception in molecular mechanical calculations. *Journal of Molecular Graphics and Modelling* **2006**, *25*, 247–260.
- (22) Case, D.; Betz, R.; Botello-Smith, W.; Cerutti, D.; Cheatham, T., III; Darden, T.; Duke, R.; Giese, T.; Gohlke, H.; Goetz, A. et al. AmberTools16. 2016.
- (23) Bekker, H.; Berendsen, H. J. C.; Dijkstra, E. J.; Achterop, S.; van Drunen, R.; van der Spoel, D.; Sijbers, A.; Keegstra, H.; Reitsma, B.; Renardus, M. K. R. Gromacs: A parallel computer for molecular dynamics simulations. *Physics Computing* **1993**,
- (24) Berendsen, H. J. C.; van der Spoel, D.; van Drunen, R. GROMACS: A message-passing parallel molecular dynamics implementation. *Computer Physics Communications* **1995**, *91*, 43–56.
- (25) Van Der Spoel, D.; Lindahl, E.; Hess, B.; Groenhof, G.; Mark, A. E.; Berendsen, H. J. C. GROMACS: Fast, flexible, and free. *J. Comput. Chem.* **2005**, *26*, 1701–1718.

- (26) Hess, B.; Kutzner, C.; van der Spoel, D.; Lindahl, E. GROMACS 4: Algorithms for Highly Efficient, Load-Balanced, and Scalable Molecular Simulation. *J. Chem. Theory Comput.* **2008**, *4*, 435–447.
- (27) Mondal, J.; Mahanthappa, M.; Yethiraj, A. Self-Assembly of Gemini Surfactants: A Computer Simulation Study. *J. Phys. Chem. B* **2013**, *117*, 4254–4262.
- (28) Martnez, L.; Andrade, R.; Birgin, E. G.; Martnez, J. M. PACKMOL: A package for building initial configurations for molecular dynamics simulations. *J. Comput. Chem.* **2009**, *30*, 2157–2164.
- (29) Sinnokrot, M. O.; Valeev, E. F.; Sherrill, C. D. Estimates of the Ab Initio Limit for Interactions: The Benzene Dimer. *J. Am. Chem. Soc.* **2002**, *124*, 10887–10893.
- (30) Chodera, J. D. A Simple Method for Automated Equilibration Detection in Molecular Simulations. *Journal of Chemical Theory and Computation* **2016**, *12*, 1799–1805.
- (31) Shirts, M. R.; Chodera, J. D. Statistically optimal analysis of samples from multiple equilibrium states. *The Journal of Chemical Physics* **2008**, *129*, 124105.
- (32) Kuriabova, T.; Betterton, M. D.; Glaser, M. A. Linear aggregation and liquid-crystalline order: comparison of Monte Carlo simulation and analytic theory. *J. Mater. Chem.* **2010**, *20*, 10366–10383.
- (33) Einstein, A. Investigations on the theory of the brownian movement. *Dover Publications* **1956**,
- (34) Liu, Y.; Zhu, F. Collective diffusion model for ion conduction through microscopic channels. *Biophys. J.* **2013**, *104*, 368–376.
- (35) Young, R.; Lovell, P. *Introduction to Polymers*, 3rd ed.; CRC Press, 2011.

- (36) Dong, R. Y.; Goldfarb, D.; Moseley, M. E.; Luz, Z.; Zimmermann, H. Translational diffusion in discotic mesophases studied by the nuclear magnetic resonance pulsed field gradient method. *J. Phys. Chem.* **1984**, *88*, 3148–3152.
- (37) Dvinskikh, S. V.; Fur, I.; Zimmermann, H.; Maliniak, A. Molecular self-diffusion in a columnar liquid crystalline phase determined by deuterium NMR. *Phys. Rev. E* **2002**, *65*, 050702.

## Graphical TOC Entry

